CMAQ MODELING AND ANALYSIS OF TRACE GASES AND BIOMASS BURNING

A Dissertation Presented to

the Faculty of the Department of Earth and Atmospheric Sciences

University of Houston

In Partial Fulfillment

of the Requirements for the Degree

Doctor of Philosophy

By

Lijun Diao

December 2016

CMAQ MODELING AND ANALYSIS OF TRACE GASES AND BIOMASS BURNING

Lijun Diao

APPROVED:

Dr. Yunsoo Choi, Chairman

Dr. Robert Talbot

Dr. Xun Jiang

Dr. Chun Zhao
Pacific Northwest National Laboratory

Dean, College of Natural Sciences and Mathematics

ACKNOWLEDGEMENTS

My special thanks go to Dr. Yunsoo Choi for his guidance and support throughout this endeavor. My sincerest appreciation goes to my committee members, Dr. Robert Talbot, Dr. Xun Jiang, and Dr. Chun Zhao for their instructive suggestions. I would also like to thank my group members of the air quality forecasting group at the University of Houston for their technical support and suggestions, without which this work would never have reached fruition. Last, but certainly not least, my deepest gratitude goes to my family members for their constant encouragement and total support in my attainment of this goal.

CMAQ MODELING AND ANALYSIS OF TRACE GASES AND BIOMASS BURNING

An Abstract of a Dissertation

Presented to

the Faculty of the Department of Earth and Atmospheric Sciences

University of Houston

In Partial Fulfillment

of the Requirements for the Degree

Doctor of Philosophy

By

Lijun Diao

December 2016

Abstract

The Community Multiscale Air Quality (CMAQ) model was extended to simulate nitrous acid (HONO) and nocturnal isoprene in Houston, and biomass burning over the United States (U.S.). The linear dependence of HONO heterogeneous reaction on the relative humidity (RH) was parameterized by scaling the reaction rate. The simulation scenarios conducted for September 2013 in Houston improved modelled-HONO concentrations and reduce the bias for NO_2 compared to observations. Similarly, simulations were conducted for nocturnal isoprene in September 2013 using the U.S. Environmental Protection Agency's (EPA's) National Emissions Inventory of 2011 (NEI 2011). The results were evaluated against measurements collected at eight Automated Gas Chromatographs sites maintained by the Texas Commission on Environmental Quality. The comparisons demonstrated an overestimation before midnight versus an underestimation after midnight. Analyses identified the underestimated wind speed as the major factor contributing to the overestimation of simulated isoprene, and uncertainties in the nocturnal isoprene anthropogenic emissions in the NEI 2011 over industrial areas in Houston as the major factor contributing to the underestimation. A sensitivity experiment with adjusted anthropogenic emissions of isoprene in the later part of the night yielded closer isoprene predictions after midnight. Finally, an offline physical plumerise module was applied to the Fire Inventory from NCAR (FINN) to simulate an intense fire episode in August 2012 in the western U.S. It was found that the base simulation with default FINN emissions underestimated the CO concentrations in the mid-troposphere. The sensitivity experiment increasing fire emissions by a factor of five improved the model simulation,

whereas the experiment reducing plume height showed little change. Modelling results indicated that during the fire event more than 40 ppb O_3 were generated near the fire sources. Three-year simulations from April to October 2012–2014 showed the contributions of biomass burning to the mean-maximum daily 8-hour (MDA8) surface O_3 and the ambient fine-particulate matter (PM2.5) was limited to regional scales. Near the fire sources, the contributions to $PM_{2.5}$ and MDA8 were more than 20 μg m^{-3} and 8–9 ppb, respectively for wildfires, and 10–12 μg m^{-3} and 3–4 ppb, respectively for prescribed fires.

Table of Contents

Chapter 1 1

1.1 Introduction 1

1.2 Methodology 3

1.2.1 Measurements 3

1.2.2 Model Setup 3

1.2.3 Parameterization of RH in the HONO Heterogeneous Reaction 4

1.3 Results 6

1.3.1 Model Evaluation 6

1.3.2 Sensitivity Tests for the Parameterization of the RH Effect on HONO Homogeneous Formation 8

1.4 Conclusions and Discussions 10

Chapter 2 11

2.1 Introduction 11

2.2 Modeling and Measurements 13

2.2.1 The Modeling System 13

2.2.2 AutoGC and Auxiliary Measurements 15

2.3 Results 16

2.3.1 Evaluation of Modeled Nocturnal Isoprene Mixing Ratios 16

2.3.2 Overestimation of Isoprene in NT1 (20:00–23:00 p.m. CDT) 18

2.3.3 Underestimation of Isoprene in NT2 (00:00–06:00 a.m. CDT) 22

2.3.4 Sensitivity Test on Anthropogenic Isoprene Emission Rate 24

2.4 Conclusions 26

Chapter 3 29

3.1 Introduction 29

3.2 Model and Data 32

3.2.1 CMAQ Model Description 32

3.2.2 Fire Plume Rise Model 34

3.2.3 FINN Biomass Burning Emission Inventory 35

3.2.4 Satellite Data 35

3.3 Results 37
3.3.1 Effect of the Emission Magnitude 39
3.3.2 Effect of the Injection Height 40
3.3.3 Impacts on Surface Ozone 41
3.4 Conclusions 42
Chapter 4 44
4.1 Introduction 44
4.2 Methodology 45
4.2.1 Model Description 45
4.2.2 Observations 46
4.3 Results 47
4.3.1 Biomass Burning Emissions in 2012–2014 47
4.3.2 Model Evaluation 47
4.3.3 Biomass Burning Contributions to $PM_{2.5}$ 50
4.3.4 Biomass Burning Contributions to MDA8 O_3 52
4.4 Conclusions 53
References 55
Appendix 1 67
Appendix 2 70
Appendix 3 74

Chapter 1

Modeling the effect of relative humidity on nitrous acid formation in the Houston area

1.1 Introduction

The Houston-Galveston-Brazoria (HGB) area is classified as a marginal ozone nonattainment area under the 2008 8-hour National Ambient Air Quality Standards (NAAQS) of 75 ppb by the U.S. EPA (http://www.epa.gov/airquality/greenbook/hnc.html). There were twenty-four ozone exceedance days in 2013 with the highest daily maximum 8-h concentration of 124 ppb at La Porte on September 25 (http://www.tceq.texas.gov). Ozone production is driven by interactions between volatile organic compounds (VOCs) and nitrogen oxides (NO_x) in the presence of sunlight. The hydroxyl radical (OH) plays a critical role in the oxidation of VOCs, particularly in urban areas (e.g., Seinfeld and Pandis, 2006; Atkinson, 2000). A significant source of OH (especially in the morning) is nitrous acid (HONO) photolysis as explained by Czader et al. (2012), Kleffmann et al. (2005), Alicke et al. (2003; 2002) and Lammel and Cape (1996).

However, current understanding of HONO formation in the atmosphere is limited due to the uncertainties related to its formation pathways and their importance in the total HONO budget. Since the well-known homogeneous HONO formation from NO and OH (reaction (R1)) is reversed in the atmosphere (Calvert et al., 1994), it is generally believed that the predominant atmospheric HONO source is the heterogeneous hydrolysis of nitrogen dioxide (NO_2) on humid surfaces outlined in reaction (R2) (e.g., Kleffmann, 2007;

Stemmler et al., 2006; Jacob, 2000; Kleffmann et al., 1998; Svensson et al., 1987; Harris et al., 1982):

$$NO + OH \rightarrow HONO \quad (R1)$$

$$2\ NO_2 + H_2O \rightarrow HONO + HNO_3 \quad (R2)$$

Evidences supporting the conversion from NO_2 to HONO have been documented by several field campaigns in the recent past (e.g., Li et al., 2012; Su et al., 2008). Other chemical sources have also been proposed—for example the gas-phase formation from photo excited NO_2 (Wentzell et al., 2010; Li et al., 2008), and the heterogeneous conversion from nitric acid on aerosol surfaces (Ziemba et al., 2010). Additionally, HONO can be directly emitted from combustion sources such as motor vehicle exhaust (Kurtenbach et al., 2001).

The heterogeneous HONO reaction (R2) has been implemented into 3-dimensional air quality models and substantially improved the simulation of HONO concentrations (Karamchandani et al., 2015; Czader et al., 2013, 2012; Foley et al., 2010; Sarwar et al., 2008). Laboratory studies have reported that the rate of HONO formation appears linear with water vapor content over a limited range of relative humidity (RH) (Finlayson-Pitts et al., 2003; Jenkin et al., 1988; Svensson et al., 1987; Pitts et al., 1984; Sakamaki et al., 1983). The water-dependence of the HONO heterogeneous reaction in the real atmosphere is as yet unclear due to the lack of comprehensive studies. Based on data from different field campaigns, Stutz et al. (2004) showed that the maximum [HONO]/[NO_2] ratio at the pseudo-steady state (PSS) linearly increased with RH, and recommended parameterizing RH in chemical transport models to accurately represent HONO formation. Tong et al.

(2015) and Hao et al. (2006) also observed that for urban and suburban regions in China, RH lineally promoted NO_2 to HONO conversion up to an RH value of 85%. Humidity in southeastern Texas is usually high, especially during summer and early fall when it can reach 80–90% during the night and early morning. Through this work (Diao et al., 2016b), we will investigate the effect of relative humidity on HONO formation, and how the incorporation of the RH dependence affects model-measurement comparison.

1.2 Methodology

1.2.1 Measurements

The study period was September 2013 when the National Aeronautics and Space Administration (NASA)'s Deriving Information on Surface Conditions from Column and Vertically Resolved Observations Relevant to Air Quality (DISCOVER-AQ) field campaign was conducted in Houston. HONO was measured on several days by an in-situ instrument, long-path absorption photometer (LOPAP) atop the University of Houston (UH)'s North Moody Tower (MT) (~70 m above ground level, AGL), 4 km southeast of downtown Houston. The accuracy of the measurements was within ± (10–15) %. A detailed description of the LOPAP apparatus was given by Heland et al. (2001). In-situ measurements of NO_2 and RH in conjunction with HONO were also obtained.

1.2.2 Model Setup

We used CMAQ model version 5.0.2 (Byun and Schere, 2006) using the Weather Research and Forecasting (WRF) model (Skamarock et al., 2008) to provide meteorological inputs. The model domain was built over 4 km × 4 km grid cells (Fig. 1.1) and 27 vertical layers. Another 12-km domain over the continental United States (U.S.)

provided initial and boundary conditions. The Carbon Bond 05 (CB05) chemistry mechanism (Yarwood et al., 2005) was chosen to represent gas-phase chemistry. Anthropogenic emission rates were taken from U.S. EPA's National Emission Inventory 2011 (NEI, 2011; http://www.epa.gov/ttn/chief/net/2011inventory.html), and model-ready emissions were prepared by the Sparse Matrix Operator Kernel Emissions (SMOKE) v3.6 model. Additional details of the modeling system were explained by Czader et al. (2015) and Pan et al. (2015). The NEI 2011 was used for the current study as compared to the NEI 2008 for theirs.

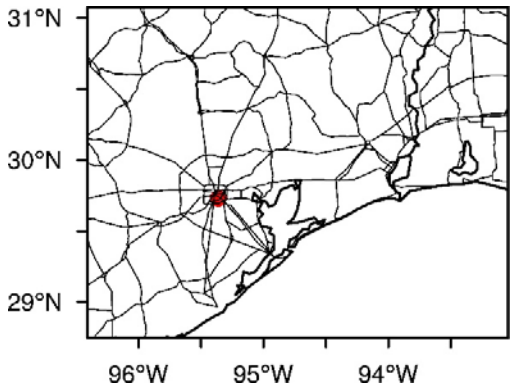

Fig. 1.1: The model domain with road map. The red dot represents Moody Tower measuring site at the University of Houston.

1.2.3 Parameterization of RH in the HONO Heterogeneous Reaction

In addition to the above mentioned reactions (R1 and R2), another gas-phase reaction forming HONO in CMAQ is:

$$NO + NO_2 + H_2O \rightarrow 2\ HONO \qquad (R3)$$

That pathway is insignificant because of its slow reaction rate (Jacob, 2000). HONO is removed via photolysis (R4) and other gas-phase reactions (R4)–(R6):

$$HONO \rightarrow NO + OH \quad \text{(R4)}$$

$$OH + HONO \rightarrow NO_2 \quad \text{(R5)}$$

$$2\ HONO \rightarrow NO + NO_2 \quad \text{(R6)}$$

The heterogeneous reaction (R2) is treated separately from gas-phase reactions in CMAQ and the product HNO_3 stays on the surface. The rate constant $k_{het} = 5.0 \times 10^{-5}(S/V)\ [s^{-1}]$ was derived by Kurtenbach et al. (2001) in a traffic-tunnel experiment, where S/V is the surface to volume ratio. The ratio takes account of both vegetation and urban structures, and varies over time and location. The readers is referred to Zhang et al. (2011) for a more detailed description of the ratio. Aerosol surfaces are included in the model separately (Sarwar et al., 2008). The urban ground surface generally provides much bigger reactive areas than aerosol surfaces. The monthly-mean aerosol concentration during the study month is 9.65 μg m^{-3} as indicated in Fig. A1.1, implying there were no highly polluted days. Two exceptional days were September 15th and 25th when the daily maximum aerosol concentrations exceeded 30 μg m^{-3} probably due to biomass burning.

Similar to the methodology of Gonçalves et al. (2012), we parameterized the RH-dependence of the heterogeneous reaction by scaling the default rate constant of the reaction (R2) by factors of RH/30 and RH/40, respectively as in Eq. (1):

$$k_{het} = 5.0 \times 10^{-5} \cdot \frac{RH}{30\ (or\ 40)} \cdot \left(\frac{S}{V}\right) \quad (1)$$

with RH in %. This approach is based on the assumption that the unknown original RH value of the tunnel experiment was around 30%. It is a reasonable assumption based on the RH values obtained from another tunnel experiment (Fujita et al., 2012). We also adopted the latest HONO/NO_x ratio of 0.016 in estimating emissions of HONO from mobile sources.

Czader et al. (2015) showed that for an urban area the new ratio brought the model prediction of HONO closer to the measurements than the previous value of 0.008.

1.3 Results

1.3.1 Model Evaluation

Since HONO formation is driven by RH and NO_2, we first assessed the model's capability of estimating meteorological variables and NO_2 against the measurements. Li et al. (2016) showed that the model reproduced the variations of meteorological fields (wind and temperature) reasonably well. Additional information about the model evaluation is in Figures A1.2–A1.3 and Tables A1.1–A1.2. Over the course of September, the weather was warm and humid, with an average temperature of nearly 300 K and the relatively humid about 75%. There were occasional showers, and the only cold front which arrived in the early morning of September 21 brought widespread light to medium rain. The model did quite a good job on RH prediction with the index of agreement (IOA) of 0.93 (Fig. 1.2 and Table 1.1). IOA, ranging from 0 to 1, takes account of both the scattering of data and biases. Refer to Czader et al. (2015) and Willmott (1981) for detailed explanations. The disparities between the model and observations principally originated from the altitude difference between the model mid-layer level and actual measurement location.

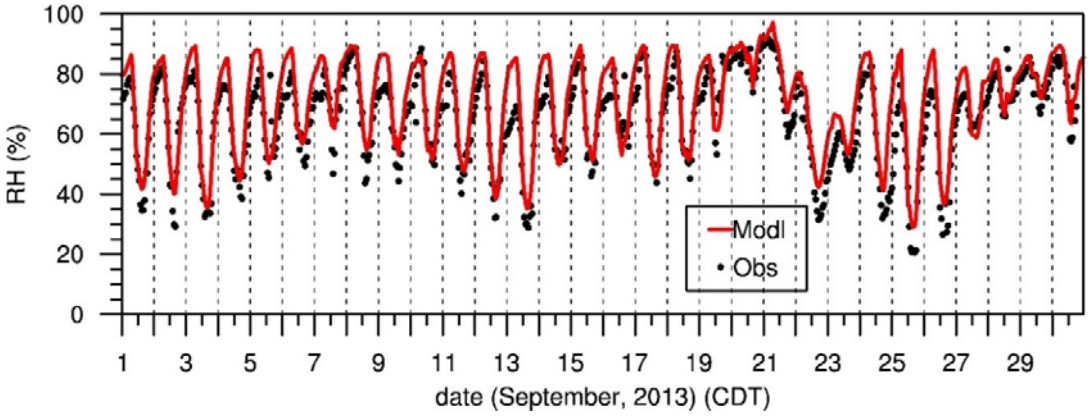

Fig. 1.2: Time series of observed and simulated RH atop Moody Tower.

Table 1.1: Statistical summary of NO_2 and RH model predictions atop MT. N represents the number of points, RHO the correlation coefficient, MML the model mean, MOB the observation mean, ME mean error, MAE mean absolute error, RMSE root-mean-squared error and IOA index of agreement of the model-measurement comparisons.

NO_2	**N**	**RHO**	**MML (ppb)**	**MOB (ppb)**	**ME (ppb)**	**MAE (ppb)**	**RMSE (ppb)**	**IOA**
Base	626	0.66	8.02	7.50	0.52	4.39	6.90	0.80
RH_30	626	0.66	7.72	7.50	0.22	4.26	6.60	0.80
RH_40	626	0.66	7.84	7.50	0.34	4.31	6.71	0.80
RH			**(%)**	**(%)**	**(%)**	**(%)**	**(%)**	
Base	714	0.91	70.92	65.64	5.28	6.27	7.81	0.93

Fig. 1.3 shows the comparison of modeled (red line) and observed NO_2 (black dots) atop Moody Tower for the simulation episode. The model mean and observation mean of NO_2 are 8.02 ppb and 7.50 ppb with a mean absolute error of 4.39 ppb. Overall the index of agreement (IOA) is 0.80 for the base case as indicated in Table 1.1, but there is a medium scatter in the corresponding scatter plot with the slope of the regression line of 0.85 and coefficient of determination R^2 of 0.45 (Fig. A1.4). The model tends to over-predict more often than under-predict and sometimes the overprediction can be more than 20 ppb, which is mainly ascribed to the uncertainties of the emission inventory (Souri et al., 2016).

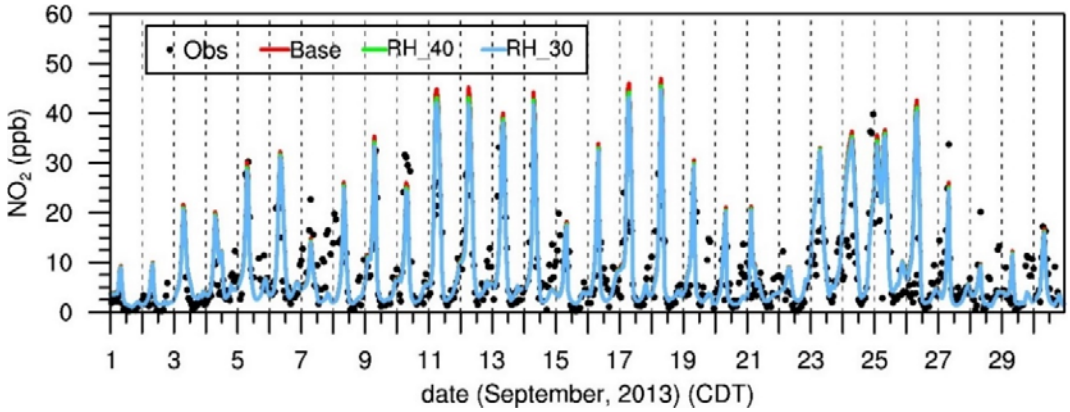

Fig. 1.3: Time series of NO_2 observations atop Moody Tower and corresponding model base and sensitivity simulations.

1.3.2 Sensitivity Tests for the Parameterization of the RH Effect on HONO Homogeneous Formation

Besides the base case simulation, two sensitivity tests, namely RH_30 and RH_40 were performed for scaling factors of RH/30 and RH/40 respectively. Fig. 1.4 shows time series of observed and modeled HONO for the base and sensitivity tests with statistics listed in Table 1.2. The base case largely under-predicted HONO with model mean of 0.24 ppb versus observation mean of 0.66 ppb. Both sensitivity tests gave considerably closer agreement with observations resulting in higher model-means of 0.51 and 0.43 ppb, respectively. The IOA of the tests are both increased to 0.78 from 0.63. The RH_40 case is considered to perform better given the least mean absolute-error in HONO.

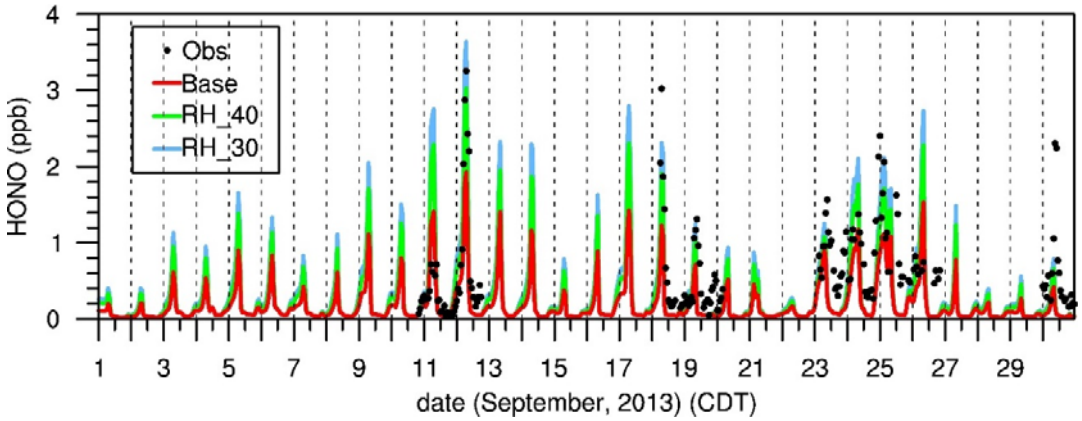

Fig. 1.4: Time series of HONO observations and model simulations of base and sensitivity tests atop Moody Tower.

Table 1.2: Statistics of HONO simulations of base and sensitivity tests.

HONO	N	RHO	MML (ppb)	MOB (ppb)	ME (ppb)	MAE (ppb)	RMSE (ppb)	IOA
Base	172	0.60	0.24	0.66	-0.43	0.45	0.64	0.63
RH_30	172	0.56	0.51	0.66	-0.15	0.42	0.60	0.78
RH_40	172	0.57	0.43	0.66	-0.23	0.39	0.56	0.78

The performance of the simulated HONO is closely associated with that of NO_2. The occasional overestimation of HONO in the early hours of the morning of September 11th and 26th could be attributed to the overprediction of NO_2. Similarly, NO_2 was over-predicted during morning rush hours on September 12th and 24th by about 20 ppb, which might help model predictions of the high peaks of HONO. On the contrary, each of the simulation cases still missed the HONO concentrations above 2 ppb during morning rush hours on September 18th and 30th when the predicted NO_2 was overestimated and approximate to the observations, respectively. Given the current systematic over-predictions of NO_2 and under-predictions of HONO, it is likely that the model could further underestimate high values of HONO when a closer agreement between modeled and

measured NO_2 was achieved. This phenomenon probably implies a potentially missing HONO source around Houston during the time as Ziemba et al. (2010) suggested.

1.4 Conclusions and Discussions

Based on the field observations of the almost linear increase in the conversion of NO_2 to HONO with vapor water content, we introduced parameterization of relative humidity for the heterogeneous reaction in the CMAQ model by scaling the reaction rate constant using factors of RH/30 and RH/40. A base-case and two sensitivity-model simulations, RH_30 and RH_40, were carried out. In the base simulation, the predicted meteorological fields showed excellent agreement with the observations. Even though NO_2, the key HONO precursor, was mostly overestimated using NEI 2011 (mean error of 0.76 ppb), the HONO concentrations were underestimated with model mean of 0.24 ppb versus observation mean of 0.66 ppb.

The two model experiments not only allowed for measurable increases in simulated HONO concentrations (model means improved to 0.51 and 0.43 ppb, respectively), but also reduced the positive biases in NO_2 slightly (mean error dropped to 0.22 and 0.34 ppb, respectively). Nevertheless, there is a need for the current model to improve NO_2 reproduction in order to predict more realistic HONO concentrations. At last, the inclusion of parameterization of relative humidity still cannot fully explain the mismatch between the modeled and observed HONO in the morning rush hours in Houston. Future work is required to focus on the physical causes behind this model-measurement disagreement.

Chapter 2

Discrepancies between modeled and observed nocturnal isoprene in an urban environment and the possible causes: A case study in Houston

2.1 Introduction

Isoprene (C_5H_8) is the most abundant biogenic volatile organic compound (VOC) with a global emission rate of 535 Tg yr^{-1} (Guenther et al., 2012). It is highly reactive with a short lifetime of ~0.5 hour (Jacobson, 2005). Therefore, it plays a vital role in tropospheric chemistry and the oxidizing power of the global troposphere (e.g., Squire et al., 2015; Poisson et al., 2000; and Wang et al., 1998). Several studies have indicated that isoprene contributed significantly to ozone formation in urban areas (e.g., Schneidemesser et al., 2011; Xie et al., 2008; Solmon et al., 2004; and Kleinman et al., 2002). Isoprene has also been recognized as an important precursor for secondary organic aerosol (SOA) (e.g., Kroll et al., 2006 and Claeys et al., 2004). While daytime isoprene concentrations have been studied thoroughly (e.g., Song et al., 2008; Li et al., 2007; and Wiedinmyer et al., 2006b), its nighttime counterpart has received little attention, especially from a model performance perspective.

The nocturnal chemistry in urban areas is dominated by the reactions of nitrogen oxides and determines the initial atmospheric chemistry conditions for the next early morning. Millet et al. (2016) observed that isoprene from a nearby forest peaked at night in an urban city and caused high ozone the next morning. The major nighttime radical, nitrate radical (NO_3), is formed via

$$NO_2 + O_3 \rightarrow NO_3 + O_2 \quad \text{(R1)}$$

and exists in equilibrium with N_2O_5. The removal of NO_3 depends on its reactions with VOCs and NO, and on the aerosol uptake of N_2O_5 (Brown et al., 2011 and Stutz et al., 2010). During the day, NO_3 quickly photolyzes under visible radiation. High uncertainties still remain regarding the nocturnal isoprene oxidation by NO_3. Model analysis showed that it contributes ~50% of the isoprene nitrates (INs), although only accounting for about 6–7% of total isoprene degradation (Horowitz et al., 2007). Those INs terminate the nitrogen cycle by producing secondary isoprene nitrate, forming SOA (1–17%), and depositing to surfaces (Mao et al., 2013 and Brown et al., 2009). Alternatively, INs recycle NO_2 by dissociation (Xie et al., 2013).

In contrast to biogenic isoprene emissions, anthropogenic emissions dominate during nighttime and daytime in cold seasons (Hu et al., 2015 and Chang et al., 2014). Sahu and Saxena (2015) even measured higher nighttime isoprene levels (mainly from anthropogenic sources) as compared to daytime levels. Anthropogenic isoprene emissions originate from several sources. For example, previous studies confirmed isoprene emissions in motor vehicle exhaust (Borbon et al., 2001; Reimann et al., 2000; and McLaren et al., 1996). The petrochemical industry manufactures isoprene as an intermediate product for the production of synthetic rubber (Chauvel and Lefebvre, 1989). Additionally, humans exhale isoprene (Buszewski et al., 2007). Wagner and Kuttler (2014) measured unusually high isoprene concentrations near a crowd.

Houston is the fourth most populous city in U.S. (http://www.census.gov/). The Houston Ship Channel (HSC) area located to the east of Houston hosts numerous

petrochemical refineries and plants. The Houston-Galveston-Brazoria (HGB) area has been designated as a marginal ozone nonattainment area by the U.S. EPA under the 2008 National Ambient Air Quality Standards (NAAQS) (https://www3.epa.gov/airquality/greenbook/hnc.html). The area experienced twenty-four ozone exceedance days in 2013 with the highest maximum daily 8-hr average (124 ppb) occurred on September 25, 2013 at La Porte, in the neighboring Galveston Bay Area southeast of Houston (http://www.tceq.state.tx.us).

This study intends to quantify nighttime isoprene concentrations in a unique urban region with a mix of traffic, industrial, and petrochemical emission sources using data from the DISCOVER-AQ aircraft campaign, which took place in September 2013 in Houston as indicated in Chapter 1. Several model studies related to air quality and meteorological issues have been carried out for this period (Diao et al., 2016b; Li et al., 2016; Souri et al., 2016; Choi and Souri, 2015; Czader et al., 2015; and Pan et al., 2015). However, to our knowledge, no model evaluation for nighttime isoprene has been conducted so far. This study will contribute a quantitative understanding of the nighttime anthropogenic isoprene emissions which could affect the urban VOC chemistry (Diao et al., 2016a).

2.2 Modeling and Measurements

2.2.1 The Modeling System

The Community Multiscale Air Quality (CMAQ) model (Byun and Schere, 2006) was used for this study. The Weather Research and Forecasting Model (WRF) (Skamarock et al., 2008) driven by the 32 km National Centers for Environmental Prediction's (NCEP's) North American Regional Reanalysis (NARR) data (Mesinger et al., 2006) provided

nudged meteorological inputs upon the Meteorological Assimilation Data Ingest System (MADIS) and Texas Commission on Environmental Quality (TCEQ) Continuous Ambient Monitoring Stations (CAMS) observations. The model domain centered in Houston (Fig. 2.1) was built over 84×66 grid cells with 4 km × 4 km grid resolution. The vertical profile consists of 27 sigma layers extending up to 100 hPa with the first midlevel height at approximately 16 m and 12 layers within 1 km. Lateral chemical boundary conditions were generated from a larger outer 12 km domain with default fixed boundary profiles. Other major WRF and CMAQ configurations are listed in Table 2.1.

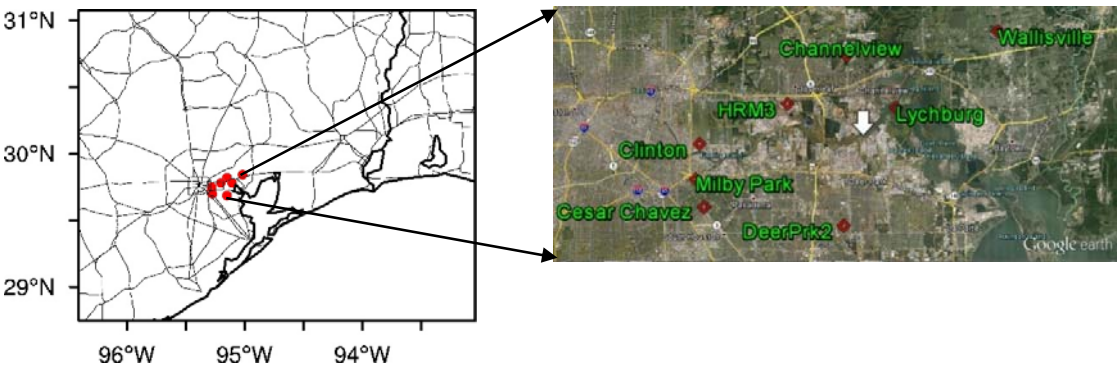

Fig. 2.1: Model domain. The red dots represent the locations of eight AutoGC sites with a close-up view on the Google map on the right. The white arrow on the Google map points to the HSC area.

Table 2.1: Selected WRF and CMAQ model physical parameterization and configuration

WRF	
Version	V3.5.1
Microphysics	Lin et al.
Long-wave	RRTMG
Short-wave	New Goddard
Surface layer	Monin-Obukhov
Land-Surface	Noah
Boundary Layer	YSU
Cumulus	Kain-Fritsch

CMAQ	
Version	V5.0.1
Gas-phase	CB05
Aerosol	AE05
Horizontal advection	Yamo
Horizontal diffusion	Multiscale
Vertical advection	WRF
Vertical diffusion	ACM2
Deposition	M3Dry

The anthropogenic emissions were prepared using the Sparse Matrix Operator Kernel Emissions (SMOKE) model based on the U.S. EPA's 2011 National Emission Inventory (NEI 2011), which consists of point, area, and mobile source categories. The anthropogenic isoprene was speciated by a source-dependent factor of the total VOC emission. Biogenic emissions were estimated from the Biogenic Emission Inventory (BEIS) model version 3.14 integrated with SMOKE. Biogenic isoprene emissions were zero at night due to their strong dependence on temperature and incident sunlight (Guenther et al., 1995). The reader is referred to Fig. A2.1–A2.2 for temporal and spatial variations of biogenic and anthropogenic isoprene emissions in and around Houston.

2.2.2 AutoGC and Auxiliary Measurements

TCEQ operates the network of Automated Gas Chromatographs (AutoGCs) in Houston to monitor a number of VOCs on an hourly basis (http://www.tceq.state.tx.us/cgi-bin/compliance/monops/agc_daily_summary.pl). One 40-minute ambient sample is collected and analyzed on-site every hour. The limit of detection (LOD) estimated by TCEQ for isoprene is 0.08 ppb. The average difference between AutoGC and canister data for isoprene concentrations is about -25% (Main et al., 2001), suggesting that isoprene concentration measured by AutoGC could be underestimated. Fig. 2.1 also shows the locations of the eight AutoGC stations: Channelview, Milby Park, Clinton, Houston DeerPrk2 (DeerPrk2), Cesar Chavez, HRM-3 Haden Road (HRM3), Lynchburg Ferry (Lynchburg), and Wallisville Road (Wallisville). Since these sites are located near industrial sources, the sampled ambient VOC levels can vary greatly depending upon wind direction. For example, Clinton is located about 800 m north of the HSC area. High

industrial VOC emitters including petroleum refineries and petrochemical plants lie to the south, southeast and east of the monitor, while residential and urban areas to the west and northwest. VOC concentrations are predominantly controlled by industrial emissions when the wind is from south and east, and by automobile emissions when the wind is westerly and northerly (Main et al., 2001). Refer to Fig. A2.3 for locations of the industrial facilities surrounding AutoGC monitors.

Simultaneous O_3, NO, NO_2, and meteorological data were obtained from TCEQ CAMS surface observations (six sites for trace gases) at the same locations as AutoGC sites. NO_2 measurements were corrected for the interference from other reactive nitrogen model species using the equation (1) in Lamsal et al. (2008). Light detection and ranging system (Lidar) was deployed at the University of Houston (UH) to measure planetary boundary layer (PBL) height during the DISCOVER-AQ campaign (Li et al., 2016).

2.3 Results

2.3.1 Evaluation of Modeled Nocturnal Isoprene Mixing Ratios

The comparison of mean diurnal variations of isoprene with observation is plotted in Fig. 2.2a (a time series plot in supplementary Fig. A2.4a). The average observed isoprene concentrations show ups and downs throughout the night but stay above 0.2 ppb. The concentrations increased noticeably for a couple of hours after 21:00 p.m. Central Daylight Time (CDT), decreased shortly after 23:00 p.m., rebounded slightly around midnight, started declining slowly for several hours after 2:00 a.m., and rose again at 6:00 a.m. They neither accumulated within the shallow nocturnal boundary layer (NBL) like other longer lifetime VOCs (e.g., xylene in Fig. 2.2e), nor decayed gradually and straightly below 0.1

ppb as observed in the rural regions (Apel et al., 2002 and Sillman et al., 2002). Although the trend is reproduced correctly, the modeled values significantly exceed measurements after dusk until 22:00 p.m., and plunge at 2:00 a.m. with large negative biases occurring before dawn. In order to investigate the influences of different processes on the results, the nighttime period was divided into two intervals: before midnight (20:00–23:00 p.m. CDT) and after midnight (00:00–06:00 a.m. CDT), namely NT1 and NT2. Table 2.2 summarizes the statistics for the simulation of nighttime isoprene. The modeled mean is 0.44 ppb versus an observed mean of 0.27 ppb in NT1, while in NT2 the model mean is 0.15 ppb versus an observation mean of 0.25 ppb. The domain-wide indexes of agreement (IOAs), values ranging from 0 to 1 and incorporating mean difference and standard deviation (Willmott, 1981), for NT1, NT2, and the entire night are 0.77, 0.66, and 0.74, respectively. The possible causes for the disparities are discussed in detail in the sections below.

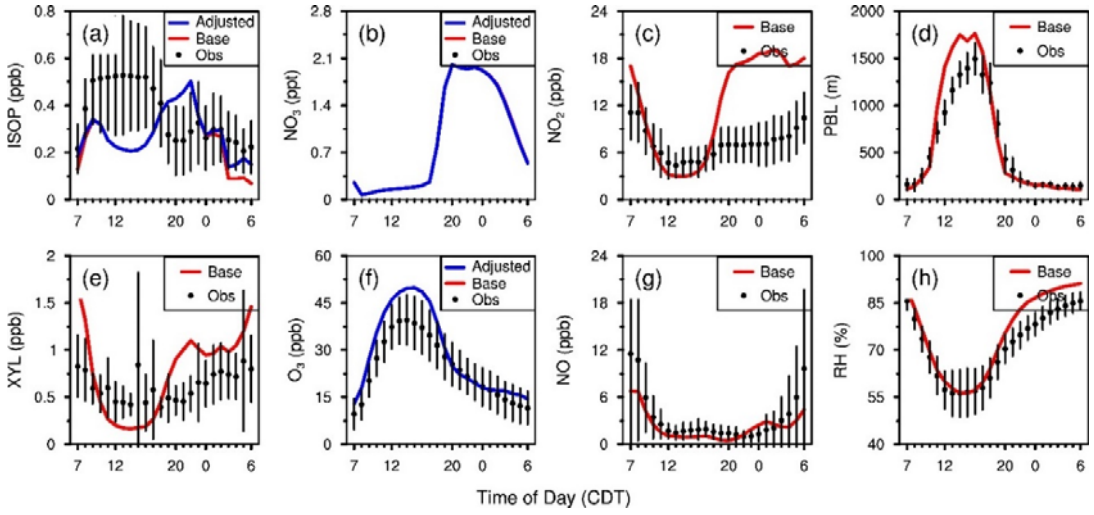

Fig. 2.2: The comparison of observed (black dots) and simulated (red line) mean diurnal variations of selected trace gases and meteorological parameters averaged at AutoGC sites in September 2013 for **(a)** Isoprene **(b)** NO_3 (no observations) **(c)** NO_2 **(d)** PBL height **(e)** xylene **(f)** O_3 **(g)** NO **(h)** relative humidity. Also shown is the simulation with adjusted

nocturnal anthropogenic isoprene emissions (blue lines) for isoprene, NO_3, and O_3. Bars represent standard deviations of the measurements.

Table 2.2: Houston AutoGC domain-wide statistical summary of the base and adjusted emission simulations of nocturnal isoprene mixing ratios, and of the base simulation of nocturnal wind. N represents the number of samples, ρ the correlation coefficient, ME the mean error, MAE the mean absolute error, RMSE the root-mean-squared error, and IOA the index of agreement. The non-shaded rows are for NT1 (or NT2) period and shaded for the whole night.

		N	ρ	Mean		Error		RMSE	IOA
				Model	Obs.	ME	MAE		
ISOP				(ppb)	(ppb)	(ppb)	(ppb)	(ppb)	
Base	NT1	249	0.37	0.44	0.27	0.17	0.25	0.38	0.77
Base	NT2	383	0.34	0.15	0.25	-0.10	0.18	0.27	0.66
Base Whole		632	0.30	0.26	0.25	0.01	0.21	0.32	0.74
Adjusted	NT1	249	0.37	0.44	0.27	0.17	0.25	0.38	0.77
Adjusted	NT2	383	0.34	0.20	0.25	-0.04	0.15	0.25	0.68
Adjusted Whole		632	0.30	0.29	0.25	0.04	0.19	0.31	0.75
Wind				(m/s)	(m/s)	(m/s)	(m/s)	(m/s)	
u-component	NT1	960	0.8	-1.0	-1.0	0.0	0.6	0.8	0.8
u-component	NT2	1677	0.8	-0.5	-0.5	0.0	0.6	0.8	0.8
u-component Whole		2637	0.8	-0.7	-0.7	0.0	0.6	0.8	0.8
v-component	NT1	960	0.7	0.7	1.0	-0.4	0.7	1.0	0.8
v-component	NT2	1677	0.9	-0.3	0.0	-0.3	0.6	0.8	0.9
v-component Whole		2637	0.9	-0.5	-0.4	-0.2	0.6	0.8	0.9

2.3.2 Overestimation of Isoprene in NT1 (20:00–23:00 p.m. CDT)

Given the short lifetime of isoprene, only small portion of isoprene emitted before dusk (e.g., before 04:00 p.m. CDT) can persist into the night (e.g., 20% left at 20:00 p.m. CDT and 0.02 ppb at 06:00 a.m. The results are from a sensitivity test turning off isoprene emissions from 04:00 p.m. to 06:00 a.m. of the following day, not shown here). Yet the modeled remnant daytime isoprene is considered unimportant in the sense that a large overestimation of isoprene occurs after dusk. Herein, we explore the other reasons covering both the atmospheric chemistry and meteorology.

Firstly, NO_3 is well known to be a significant sink of isoprene after dark (Stutz et al., 2010 and Perring et al., 2009). The simulated nighttime NO_3 mixing ratios (Fig. 2b) quickly rise after sunset (~ 19:25 CDT) and fall at a similar rate after 02:00 a.m. CDT. The maximum mean-value is only ~2 ppt with the highest concentration up to ~10 ppt occurred on an O_3 event day (Fig. A2.4b). The monthly mean approximates the value from the global model STOCHEM (Khan et al., 2015). As an observation reference, NO_3 concentrations up to 149 ppt were observed near the surface in Houston during the 2006 TexAQS field study (Stutz et al., 2010). Unfortunately, no NO_3 measurements are available for the DISCOVER-AQ Houston campaign. However, there are other pointers. Owing to the EPA's State Implementation Plan (SIP) call, the national NO_x emissions in U.S. have declined by ~24% during the past decade as estimated from the NEI 2011 emission inventory. Also, NO_3 mixing ratios were consistently below 1 ppt during the Southern Oxidant and Aerosol Study (SOAS) campaign in summer 2013 in central Alabama, home to a number of power plants (Ayres et al., 2015). In addition, the modeled NO (one of major sinks of NO_3) agrees well with observations except around dawn (Fig. 2.2g), whereas the modeled NO_2 (main source of NO_3) deviates significantly from observations at night (Fig. 2.2c) because the simulation of short-lived NO_2 strongly depends on the emission inventory (Souri et al., 2016). Hence, we suspect that the model has slightly more NO_3 than the actual concentrations. That would lead to a small underprediction of isoprene (τ = 8 hr at $[NO_3]$ = 2 ppt; Burkholder et al., 2015).

Secondly, vertical convection was apparently absent since most nights of the month were clear and calm ($u < 1$ m s^{-1}) except in the early morning of September 21 when a cold

front passed to the east. Consequently, a strong nocturnal temperature inversion up to ~370 m was prevalent near the ground revealed by the modeled mean nocturnal vertical temperature profile in Fig. 2.3a. In the WRF model, the Yonsei University (YSU) PBL scheme represents the NBL height reasonably well as shown in Fig. 2.2d. Additionally, the vertical diffusion scheme in the CMAQ model appears to work well since the surface O_3 in Fig. 2.2f (time series plot in Fig. A2.4c) is close to measurements (Tang et al., 2011). Note that the positive biases of O_3 become progressively larger after midnight when the decreasing temperature raises relative humidity (Fig. 2.2h). The problem is similar to that noticed by Park et al. (2014) when evaluating the dry deposition scheme of the CMAQ modeling system and requires further investigation (Zhang et al., 2003). Fig. 2.3b manifests the simulated average-nocturnal vertical profile of isoprene with a deep gradient within the NBL, which can be mainly attributed to that of NO_3 in Fig. 2.3c. In reality, the observed NO_3 mixing ratio did continuously increase with height (Brown et al., 2007) away from the source region. Furthermore, the model underestimated the daytime isoprene vertical distributions especially below 1 km in the urban (Moody Tower) and suburban (Channelview) regions during the DISCOVER-AQ campaign, whereas it performed much better over the rural Conroe area (Fig. 2.4). Based on these findings, we inferred that the nighttime isoprene vertical profile was likely underestimated due to its daytime counterpart. But in the poorly mixed NBL, the influence of vertical transport on surface isoprene was supposed to be small.

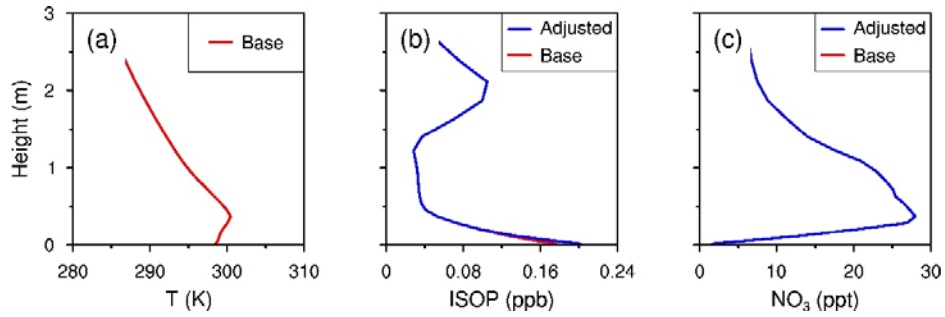

Fig. 2.3: Temporal mean modeled vertical profiles of **(a)** air temperature **(b)** isoprene **(c)** NO_3 at night, averaged over AutoGC sites.

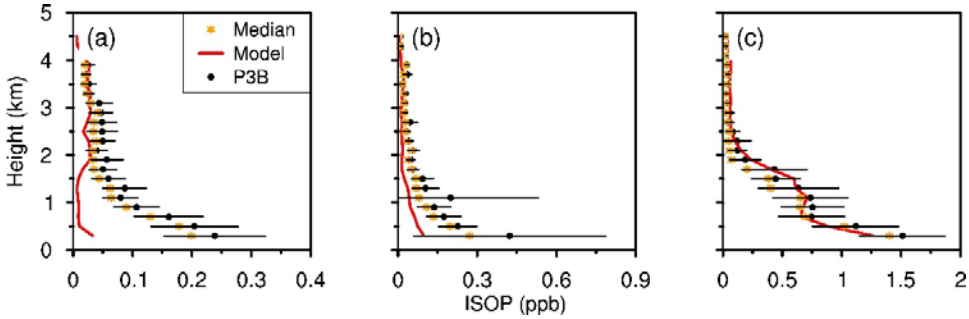

Fig. 2.3: Average daytime isoprene vertical profiles (black dots) (nine flight days and three times of sampling a day around morning, noon, and afternoon) from NASA DISCOVER-AQ field campaign with the model simulation (red line) for aircraft spirals at **(a)** Moody Tower of UH **(b)** Channelview **(c)** Conroe. Bars and orange asterisks represent one standard deviation and median of the binned observations at each 0.2 km interval respectively.

Lastly, the statistics of the simulated nocturnal wind are provided in Table 2.2 (Time series plot in Fig. A2.4d–e). The WRF model shows IOAs of 0.8, indicative of a good performance of nocturnal-surface wind fields. However, the wind speed, especially the v-component (model mean of 0.7 m s^{-1} versus observation mean of 1.0 m s^{-1}), was under-predicted during NT1. By contrast, Ngan et al. (2013) showed the over-prediction of nocturnal wind speed of June 2006 in the HGB region. But their attempts to minimize the errors failed despite improvements in the prediction of surface temperature and sensible

heat flux. Since isoprene concentration correlates negatively with wind speed less than 4 m s^{-1} (Liakakou et al., 2007), the wind speed is the most likely cause of the overestimation of isoprene after sunset.

2.3.3 Underestimation of Isoprene in NT2 (00:00–06:00 a.m. CDT)

As mentioned above, the biases between modeled and measured mean surface-isoprene mixing ratios become negative and pronounced after midnight. Although NO becomes largely underestimated before dawn which aggravates the over-prediction of NO_3 and underestimation of isoprene, NO_3 kept decreasing in this period until the value was below 1 ppt. Also, its production from O_3 was slow (reaction rate constant is equal to 3.2 $\times 10^{-17}$ cm^3 $molecule^{-1}$ s^{-1} at 298 K; Burkholder et al., 2015). Additionally, the wind speed tends to be over-predicted to a minor extent in this period when the in-situ wind slowed down. Thus, the aforementioned reasons cannot fully explain the large negative biases in surface isoprene in this period. Ozonolysis is also easily excluded given the relatively long isoprene lifetime of ~1.3 days with respect to O_3 (Pacifico et al., 2009). We noticed there were frequent upturns in isoprene mixing ratios during the night, in tandem with other anthropogenic VOCs. As an extreme example, isoprene reached its daily maximum of 0.98 ppb one hour before the peaks of several other VOC species such as toluene and n-hexane at Channelview at 3:00 a.m. on September 10, when the wind blew from the north where large industry facilities are located.

Given the short lifetime of isoprene, 6-hour HYSPLIT (HYSPLIT, 2015) back-trajectory modeling for trajectories ending at 00:00, 03:00 and 06:00 a.m. was conducted. The plot in Fig. 2.4 indicates that the air masses arriving at AutoGC sites at the time are

mostly local as expected. The wind-rose plots in Fig. 2.5a and b show that during most of the night, the wind veered back from southeast to northeast as part of the local sea-land breeze cycle. The wind pattern is reasonably well captured as shown in Fig. 2.5c and d. The changing of wind direction made the AutoGC sites downwind of some industrial facilities. Similarly, Leuchner and Rappenglueck (2010) assigned winds from the first quadrant primarily to transporting industrial emissions when determining source apportionment of VOCs at AutoGC sties. Moreover, marine isoprene produced from phytoplankton species is estimated to be very low (1.6–10 pptv) (Gantt et al., 2010 and Matsunaga et al., 2002). Therefore, we determined that the large negative biases of isoprene concentrations after midnight were mainly caused by the underestimation of the nocturnal anthropogenic-isoprene emissions.

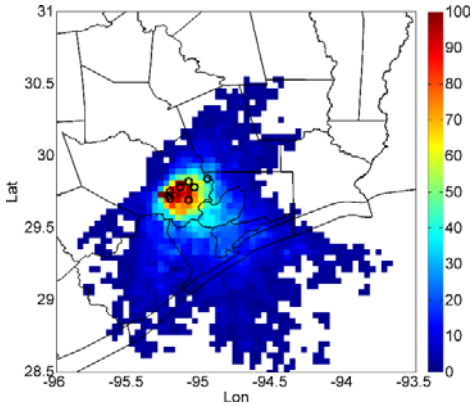

Fig. 2.4: Frequency map of the HYSPLIT 6-hr backward trajectories ending at 0:00, 3:00, and 6:00 a.m. (CDT) arriving at AutoGC sites (black circles).

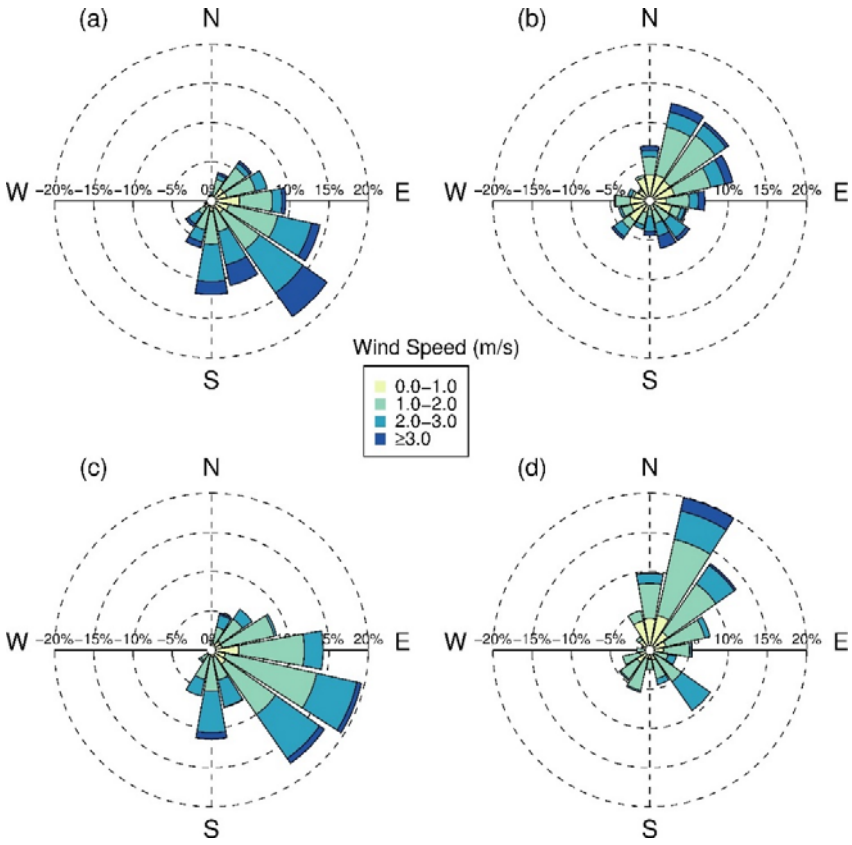

Fig. 2.5: Wind-rose of modeled and observed nocturnal hourly data at AutoGC stations. **(a)** Observed in NT1; **(b)** observed in NT2; **(c)** modeled in NT1; **(d)** modeled in NT2.

2.3.4 Sensitivity Test on Anthropogenic Isoprene Emission Rate

We conducted a sensitivity test in which anthropogenic isoprene emission rates from SMOKE during 1:00–6:00 a.m. CDT were scaled using the hourly correction factors described below:

Adjusted emission rate = base emission rate × hourly factor

These factors were obtained by averaging the observed-to-simulated ratios under light wind conditions (wind speed < 2 m s^{-1}) within each hour. We assumed that the emission rate was proportional to the surface concentrations of isoprene. Table 2.3 lists the underestimation

factors for model grid cells where the monitoring stations are located and the domain-wide average factors applied to the other grid cells. The anthropogenic isoprene-emission rates in NT1 remain unchanged because the relatively large uncertainties of the simulated wind speed make it difficult to get reasonable factors.

Table 2.3: Mean hourly factors of AutoGC isoprene measurements to model data during 1:00–6:00 a.m. under low wind speed conditions (< 2 m s^{-1}). N is the summation of number of valid samples, and the percentage is the percent of N of the number of total samples. Milby Park and Cesar Chavez share the same average factors due to their collocation in the same model grid cell.

Station Name	**Hourly Factors**							
	01:00	02:00	03:00	04:00	05:00	06:00	N	%
Channelview	4.33	9.57	31.56	35.49	19.24	32.32	56	97
Milby Park	1.43	4.26	5.83	4.11	5.79	9.77	13	100
Clinton	2.23	3.61	4.02	4.79	4.06	4.60	31	89
DeerPrk2	4.04	5.39	4.78	0.70	9.35	10.02	21	100
Cesar Chavez	1.43	4.26	5.83	4.11	5.79	9.77	63	98
HRM3	8.49	3.00	9.57	9.11	8.71	6.49	49	92
Lynchburg	7.80	2.70	31.20	18.14	9.68	31.81	14	33
Wallisville	0.72	0.59	5.17	20.13	7.82	13.76	32	84
All	3.81	4.17	12.25	12.07	8.81	14.82	279	86

The results of the sensitivity simulation are shown in Fig. 2a, b, and f (time series in Fig. A2.4a–c) and Table 2.2 as the adjusted emission case. The underestimation of the base simulation in NT2 becomes less severe with increased model mean of 0.20 ppb and reduced mean absolute error of 0.15 ppb, resulting in a slightly improved IOA from 0.66 to 0.68 for NT2 and 0.74 to 0.75 for the entire night. The only slight improvement likely results from the simple assumption of the linear relationship between emissions and concentrations, and the uncertainties of the spatial distribution of the anthropogenic emissions. More observational data needs to be available over the HSC and neighboring areas to mitigate these uncertainties. The adjusted isoprene-emission rates raised the

monthly mean concentrations of the isoprene oxidation products, namely methacrolein (MACR) and methyl vinyl ketone (MVK), gas phase organic nitrates (NTR) (time series plots in Fig. A2.5) and O_3 by 2.57, 1.79 and 3.20 ppt, respectively.

2.4 Conclusions

Our results showed significant error between the CMAQ model predictions of ground-level nocturnal isoprene concentrations and the TCEQ AutoGC measurements for September 2013. The mean observed nocturnal isoprene concentrations stay above 0.2 ppb the entire night with a pronounced peak before midnight, a small rebound around midnight, and then a slow descent till dawn. The model over-predicted the magnitude of the isoprene increase after sunset and the decline rate during early morning hours. In order to identify the sources of the model-measurement error, we investigated a few sources of uncertainties, namely: (1) the nighttime chemistry related to NO_3, (2) vertical transport, (3) wind fields, and (4) anthropogenic isoprene source emissions.

Because of the overabundance of nighttime NO_2, NO_3 is likely overestimated which favors an opposite trend for its major loss contributor, isoprene. The magnitude of that impact is small due to the very low concentrations of modeled NO_3 (~2 ppb on average). Verifying this argument needs NO_3 measurements which were unfortunately not recorded as part of the DISCOVER-AQ campaign. An additional minor sink of surface isoprene at night with limited vertical mixing might be introduced by the possibly underestimated nighttime isoprene-vertical distribution, suggested by its underestimated daytime counterpart in urban Houston. On the other hand, the over-prediction of isoprene mixing ratios after sunset is very likely related to the relatively large underestimation of the v-

component of the wind, even though the model achieved a good performance of nocturnal u- and v-wind components with IOA values of 0.8 and 0.9, respectively during the whole night.

Furthermore, we examined how the changes in the wind pattern affect nighttime isoprene concentrations. The nighttime isoprene frequently increased especially after midnight and the timing was coincident with the changes in wind direction. At night, the origin of the wind generally changed from southeast to northeast making the eight AutoGC stations downwind of industrial facilities. This leads to the possibility that the underestimation for nocturnal isoprene is mainly due to that in anthropogenic isoprene emissions. Average hourly correction factors during 1:00–6:00 a.m. ranging from 3.81 to 14.82 were obtained from the mean ratios of the observed to simulated nighttime isoprene concentrations at AutoGC sites. The sensitivity test using the anthropogenic isoprene emission rates adjusted by those factors produced slightly better nocturnal isoprene concentrations in the later part of night (NT2). The model mean changed from 0.15 to 0.20 ppb, mean error from -0.10 to -0.04 ppb, mean absolute error from 0.18 to 0.15 ppb, and IOA from 0.66 to 0.68. The adjustment makes negligible impacts on isoprene oxidation products—methacrolein and methyl vinyl ketone, organic nitrates, and ozone. The modest improvements of the nighttime isoprene simulation likely were resulted from the uncertainties of the locations of high-peaked anthropogenic emissions from NEI 2011 and the simple linear assumption between emissions and concentrations. More in-situ measurement sites and data are needed to constrain anthropogenic isoprene emissions in Houston.

Further improvement can be achieved by using a higher model resolution since Milby Park and Cesar Chavez collocate in the same model grid cell but had different observation readings. Using a higher modeling resolution of 1 km could differentiate simulated isoprene concentrations at these two stations. Another necessary study under planning is to improve daytime isoprene emissions/concentrations using a new version of the biogenic emission inventory system and inverse modeling approach based on aircraft isoprene, HCHO and CO measurements and remote-sensing data, in particular OMI HCHO and MOPITT CO (e.g., Choi and Souri, 2015 and Choi et al., 2010).

Chapter 3

Model sensitivity studies of the long-range transport of wildfire smoke from western United States

3.1 Introduction

Biomass burning (BB), the combustion of vegetation over a large area of land, includes forest fires struck by lightning and prescribed agricultural burning. Devastating wildfires cause visibility degradation (Levin et al., 2010), property damage, and casualties (Akagi et al., 2011). A previous study suggested that particle emissions from burning sugar cane impaired the respiratory system of children and the elderly (Cançado et al., 2006). BB is a major source of trace gases and particulate matter in the global atmosphere (Andreae and Merlet, 2001). The emissions not only deteriorate the air quality in local and downwind regions, but also travel hundreds and thousands of kilometers, impacting tropospheric chemistry on the hemispheric scale (Novelli et al., 2003).

A number of studies have been carried out to simulate the effects of fires around the globe (e.g., Field et al., 2016; Walter et al., 2016; Fu et al., 2012; Sessions et al., 2011; In et al., 2007; Pfister et al., 2006; and Jaffe et al., 2004). Accurate model simulation of transport and transformation of BB emissions is challenging for three reasons. Firstly, considerable discrepancies appear among various fire-emission estimates. The well-known Global Fire Emissions Database (GFED) (van der Werf et al., 2010) version 3.1 agrees well with the Fire Inventory from NCAR (FINN) version 1.0 for the global annual CO_2 emissions, but they differ by about four times over specific regions (Wiedinmyer et al.,

2011). Parrington et al. (2012) suggested scaling of the Fire Locating And Monitoring of Burning Emissions (FLAMBE) by 12%–102% based on the adjoint inversion of CO emissions from satellite measurements. Inter-comparison of four top-down constrained monthly BB emissions revealed differences up to a factor of 10 (Al-Saadi et al., 2008). Additionally, the temporal resolution of a BB inventory matters too. Fire activities were observed to peak in the afternoon (Giglio, 2007) and exhibit a strong diurnal cycle (Prins and Menzel, 1992) influenced by weather and fuel conditions (Andela et al., 2015). Chen et al. (2009) and Field et al. (2016) demonstrated that emissions at finer temporal resolution altered spatial distribution patterns for pollutants and the synoptically resolved emissions resulted in more pollutants injected to higher altitudes.

Another reason for the uncertainties in BB simulation is that quantitative determination of smoke-injection height is not straightforward. Large variability exists in smoke-injection heights ranging from a few hundred meters to about 4.5 km above the terrain (Kahn et al., 2008). The injection height determines smoke transport distance and direction. Leung et al. (2007) indicated that higher smoke-injection height produced larger ozone enhancement downwind. Given the complexity of the dynamic evolution of BB plumes, a simplified approach in CTMs is to distribute fire emissions uniformly within the planetary boundary layer (Parrington et al., 2012) or below given height (Pfister et al., 2006). By analyzing the stereographic plume heights for 2002 and 2004–2007 seen from the Terra Multi-angle Imaging SpectroRadiometer (MISR), Val Martin et al. (2010) have found that about 4–12% of fire plumes over North America reached the free troposphere. An empirical parameterization developed by the Western Regional Air Partnership (WRAP)

(Tai et al. 2008; WRAP, 2005) estimates hourly top and bottom heights of the elevated plume according to its aggregated area burned category. The WRAP scheme assumes all nighttime fire emissions to be injected in the first model layer, which may lead to the overestimation of ground level BB impacts near the fire source regions. Another empirical plume rise model, BlueSky based on the Briggs equations (Briggs, 1975), was implemented into the SMOKE (SMOKE, 2016). Although suitable for controlled fires, BlueSky was not capable to predict wildfire behaviors (Paugam et al., 2016) because it generally underestimates smoke injection heights compared with satellite measurements (Raffuse et al., 2012). Freitas et al. (2007) developed a 1-dimensional dynamic plume module taking into account of the driving forces of pyro-convection. The approach has been adopted by the Weather Research and Forecasting model coupled with Chemistry (WRF-Chem) to treat fire emissions. More detailed description about the module is provided in the following section.

Finally, the knowledge about the vertical distribution of the fire emissions is limited because of sparse field measurements. Several researchers (Walter et al., 2016; Sofiev et al., 2013; Gonzi and Palmer, 2010) derived vertical profiles relying on hypothesis or satellite observations, creating inconveniences for practical use. As mentioned above, distributing fire emissions uniformly is a common alternative approach. Nevertheless, the vertically non-uniform nature of fire has been identified and the upper flaming and bottom smoldering combustion phases have been addressed (Pouliot et al., 2005).

Fires are projected to occur more frequently in a future warmer climate (Daniau et al., 2012). The Intergovernmental Panel on Climate Change report (IPCC, 2013) ranks

biomass burning among the larger contributors to global warming over the next 50 to 100 years. It is in urgent need to quantify the impacts of biomass burning on the Earth's atmosphere and climate system. This study integrated the aforementioned physical plume rise module into the CMAQ model to investigate an intense wildfire event that occurred in the summer 2012. The year of 2012 is the hottest year in the continental U.S. in the recent decade (Melillo et al, 2014) associated with extensive drought, which resulted in $31.5 billion economic losses (NOAA, 2012a). During August–September 2012, the highest wild fire activities over the last decade since 2002 in the western U.S. (McDonald-Buller et al., 2015) burned nearly 19,078 km^2 (NOAA, 2012b), about the land area of South Dakota, and cost $1.5 billion and eight deaths (NOAA, 2012a). Despite the damages suffered by the region, this event provides a good opportunity to assess the performance of the chemical transport models (CTMs) in predicting the influences of biomass burning and transport of chemical tracer compounds.

3.2 Model and Data

3.2.1 CMAQ Model Description

The offline CMAQ model (Byun and Schere 2006) version 5.0.2 was employed for this study. Gas-phase chemistry was simulated by the Carbon Band 05 (CB05) mechanism (Yarwood et al., 2005) with active chlorine and updated toluene mechanisms. Aerosol chemistry was simulated by the aerosol module, version 6 (AE6). Emissions were prepared by the Sparse Matrix Operator Kernel Emissions (SMOKE) modeling system, in which the anthropogenic emissions are based on the 2011 National Emission Inventory (NEI). The meteorological inputs were provided by the Advanced Weather Research and Forecasting

Model (ARW-WRF) version 3.7 (Skamarock et al., 2008) driven by the National Centers for Environmental Prediction (NCEP) North American Regional Reanalysis (NARR) data (Mesinger et al., 2006). The model configuration is summarized in Table 3.1. Fig. 3.1 shows the model domain covering the continental U.S. and parts of Canada and Mexico. The color shadings delineate terrain height. The domain was built over 12 km × 12 km grid cells. The vertical grid of WRF consists of 28 sigma levels extending up to 100 hPa. To save computation time, the meteorological inputs for CMAQ, processed by the MCIP program, only have 15 vertical layers with the first midlevel height at approximately 15 m and 8 layers within 1 km. To replace the default temporally-static chemical-lateral boundary profiles, $2^0 \times 2.5^0$ grid resolution GEOS-Chem global chemical transport model were carried out in which the biomass burning emissions from FINN were uniformly distributed within the planetary boundary layer (Bey et al., 2001).

Table 3.1: Selected WRF and CMAQ model physical parameterization and configuration

WRF	
Version	V3.5.1
Microphysics	Lin et al.
Long-wave Radiation	RRTMG
Short-wave Radiation	New Goddard
Surface layer	Monin-Obukhov
Land-Surface	Noah
Boundary Layer	YSU
Cumulus Convection	Kain-Fritsch
CMAQ	
Version	V5.0.2
Gas-phase Mechanism	CB05
Aerosol	AE06
Horizontal advection	Yamo
Horizontal diffusion	Multiscale
Vertical advection	WRF
Vertical diffusion	ACM2
Deposition	M3Dry

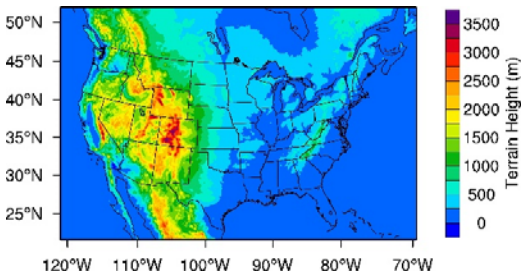

Fig. 3.1: Model domain. Color contour shows terrain height (m).

3.2.2 Fire Plume Rise Model

Similar to Raffuse et al. (2012), in this study plume top and bottom define a vertical zone within which the smoke begin to transport away from the source region. The terminal height of smoke depends on several factors including atmospheric static stability, water vapor content, wind speed and heat flux released by the fire (Freitas et al., 2007). On average, pyrogenic trace gases and aerosols in an unstable air mass can be lifted ~600 m higher than those in a stable one (Val Martin et al., 2010). The latent heat from condensation of water vapor adds buoyancy to the lofted smoke (Penner et al., 1986). Strong horizontal wind causes greater entrainment, lowering down the plume height, and bends the smoke too (Freitas et al., 2010). Therefore, an accurate plume rise model considering those physical processes is necessary to distribute fire emissions vertically in the CTMs. We adopted the 1-D plume rise model developed by Freitas et al. (2007), which explicitly treats the pyro-convection by solving equations of vertical motion, the first law of thermodynamics, and continuity of water vapor through iteration. The model obtained environmental conditions from the host model and returned the final plume top and bottom heights. The fire emissions were then evenly distributed within the plume layer for each

type of vegetation and scaled by a calculated factor between the flaming and smoldering combustion.

3.2.3 FINN Biomass Burning Emission Inventory

FINNv1.5 provides global emissions of trace gases and particles from BB (Wiedinmyer et al., 2011) (available at http://bai.acom.ucar.edu/Data/fire/). Compared with the 0.25^0 (~27.5 km) special resolution of GFEDv4s, FINN is unique in its high spatial resolution of 1 km and daily temporal resolution. The fire pixel is identified by the MODIS Thermal Anomalies Product (Giglio et al., 2006). The land cover/land use (LULC) and vegetation density within each fire pixel are determined by the MODIS Land Cover Type (LCT) (Friedl et al., 2010) and Vegetation Continuous Fields (VCF) products (Carroll et al., 2011; Hansen et al., 2005; Hansen et al. 2003), respectively. The area burned is set to be an upper limit for each generic LULC and scaled based on VCF data (Wiedinmyer et al., 2006a). Model-estimated fuel loading is assigned for each land cover type. The fraction of biomass burned within a fire pixel is related to its tree coverage. Emission factors of species are collected from literatures. We adopted emissions speciated for the MOZART-4 chemical mechanism (Emmons et al., 2010) and mapped to CB05 mechanism according to Tai et al. (2008) (Table A3.1). Then the emissions were re-gridded to the model domain and allocated to a diurnal cycle using the fire_emis tool provided along with the inventory from the developer.

3.2.4 Satellite Data

The swath CO mixing ratio profiles from the Atmospheric Infrared Sounder (AIRS) onboard NASA's Aqua satellite was selected for comparison to model results. The satellite

was launched on May 4, 2002. Flying at an altitude of 705 km above the Earth surface, the satellite is in polar sun-synchronous orbit, passing equator at local time 1:30 p.m. local time (LT) in the ascending node. The 1650 km swath width enables global coverage in a day. The footprint size is 13.5 km at nadir. CO is retrieved from 4.5 μm thermal infrared-spectral region (McMillan et al., 2005). The latest version 6 level 2 standard products include 28 pressure levels from 1100 to 0.1 hPa. The comparisons of the satellite CO measurements from AIRS and Measurement of Pollution in the Troposphere (MOPITT) on NASA's Terra satellite were reasonably well (Yurganov et al., 2008; Warner et al., 2007).

The Multi-angle Imaging Spectroradiometer (MISR) onboard the Terra satellite provides valuable observations for smoke injection height. Akin to Aqua, Terra began collecting data on February 24, 2000. It passes the equator at 10:30 a.m. LT in the descending node. Distinct from most satellite instruments, MISR views the Earth's surface at nadir, forward and aftward angles of $\pm 26.1^0$, $\pm 45.6^0$, $\pm 60.0^0$, and $\pm 70.5^0$ along the spacecraft track with nine cameras. Each camera has four wavelengths, blue, green, red, and infrared. Swath width is 360 km in order to achieve global coverage in 9 days. MISR revisits the same location in 2 to 9 days depending on latitude. The spatial resolution at nadir is 250 m, and 275 m at all off-nadir angles. The MISR Interactive eXplorer (MINX) software allows the user to interactively digitize the smoke shape and wind direction on the terrain-referenced imagery. Wind-corrected smoke height is computed by a geometric, stereoscopic method at 1.1 km spatial resolution. The readers are referred to Nelson et al. (2013) and Kahn et al. (2008) for more details about the retrieval.

3.3 Results

During August 2012, a series of wildfires were burning in north California, Oregon, Nevada, and Idaho (MTBS website). Among them, each of the three large fires, the Mustang Fire, Halstead Fire, and Trinity Ridge Fire, scorched more than 58,000 ha (580 km^2) in the middle of Idaho (Ryan and Opperman, 2013). The Holloway Fire is the second largest fire in Nevada history (NIFC, 2016). Fig. A3.1 depicts Aqua/MODIS true color images acquired in the period of August 14–16, 2012. Grey smoke from the western U.S. wildfires can be seen drifting eastward.

AIRS observed widespread elevated levels of CO in the western U.S. fire regions and their eastward transport at 500 hPa shown in Fig. 3.2. The left panel of Fig 3.2 shows that CO concentrations around 300 ppb were accumulating in southeast Idaho on Aug 14. In the panel (a) of the Fig. A3.1, thick smoke blown by the northwesterly wind (Fig. 3.3 (a)) appeared across Wyoming, the location of the gap between AIRS granules. At 20:00 UTC (Universal Time Coordinated) next day, the fire plume advanced eastward reaching the South Dakota-Nebraska border and spread to Kansas with the aid of the northwesterly wind shown in Fig. 3.3 (b). At 8:00 UTC on August 15, the smoke with the similar amount of CO as previous days made its way to the Great Lakes region under the west wind near the base of the trough in Fig. 3.3 (c). The corresponding model simulations with default BB emissions are presented in Fig. 3.4. Although the model captured the trajectory well (easily seen in the concentration difference plot in Fig. A3.2), the magnitude of CO enhancement was underestimated. In Fig. 3.4, no plume is apparently heading towards east. Over southeast Idaho the peak value is only ~150 ppb modeled versus ~350 ppb observed.

To improve model performance, two sensitivity tests have been performed for the magnitude of emissions and plume injection height. Henceforth, the simulation with default BB emissions will be referred as the base BB case.

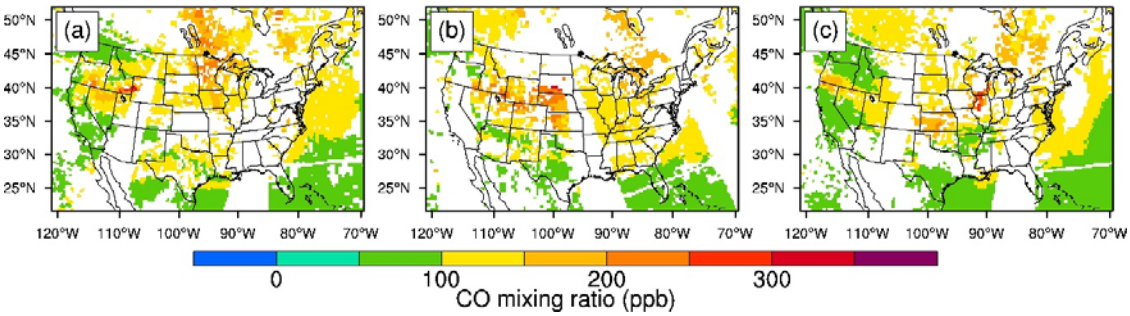

Fig. 3.2: AIRS CO VMRs (ppb) at 500 hPa in the **(a)** nighttime of Aug 14, 2012 **(b)** daytime of Aug 15, 2012 **(c)** nighttime of Aug 16, 2012.

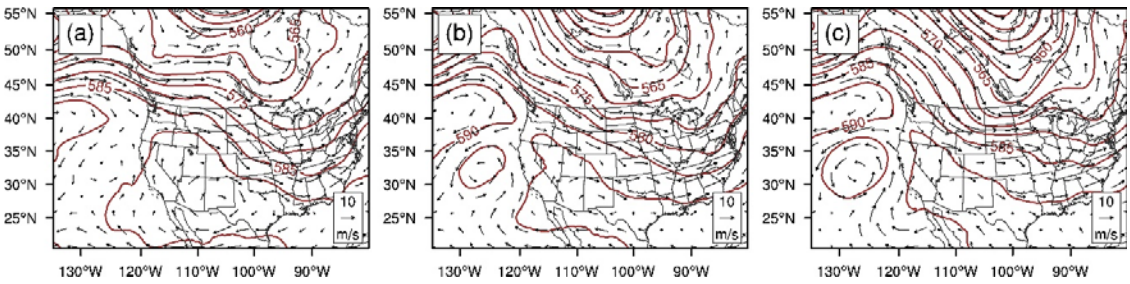

Fig. 3.3: Mean 500 hPa geopotential height (dam) and winds (m/s) for **(a)** 10:00Z Aug 13–10:00 UTC Aug 14, 2012 **(b)** 10:00 UTC Aug 14–20:00 UTC Aug 15, 2012 **(c)** 20:00 UTC Aug 15–8:00 UTC Aug 16, 2012. Each end time corresponds to the AIRS passing time over the peak values of the transported eastward CO in Fig. 3.6. The NCEP Reanalysis data is provided by the NOAA/OAR/ESRL PSD, Boulder, Colorado, USA, from their web site at http://www.esrl.noaa.gov/psd/.

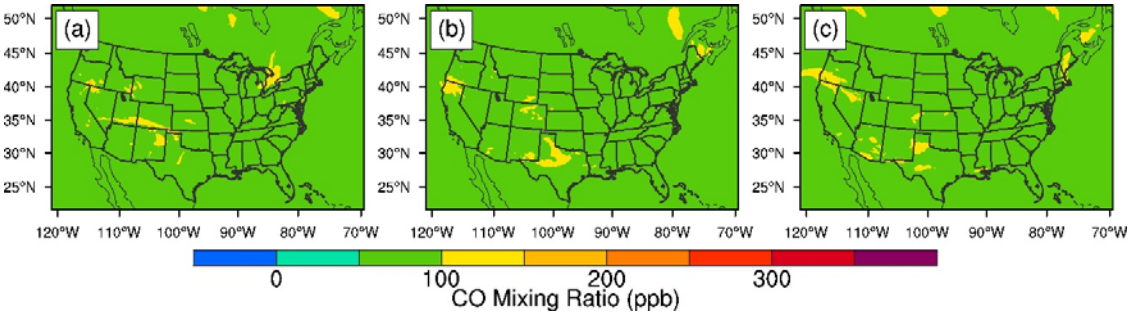

Fig. 3.4: CMAQ simulated CO concentrations with BB emissions at 500 hPa at the same time as the end time of each period in Fig. 3.3.

3.3.1 Effect of the Emission Magnitude

As discussed earlier, the estimation of BB emissions is tied to great uncertainties. According to McDonald-Buller et al. (2015), FINN emission inventory has 42% low bias over U.S. mainly due to the uncertainties in the algorithm to determine the burned area. Compared to the MODIS/Terra thermal anomaly data v6, it was found that the FINN emission model largely ignores the number of fire spots in some cases (not shown). In addition, it was noticed that the base biomass burning simulation significantly under-predicted CO concentrations obtained during the Deep Convective Clouds and Chemistry (DC3) field campaign when the High Park wildfire in Colorado aggressively expanded to a new regime (not shown). Since Aqua overpasses the same location twice a day, it is easy to miss abrupt fire variations. Per the preceding reasons, the FINN emissions were multiplied by a factor of five. The results of the new simulation are displayed in Fig. 3.5. The CO enhancement at 500 hPa increased abreast of the measurements. However, even though the highest concentrations are overestimated near the fire sources on August 14, they are still underestimated on the following days. Also, the peak concentrations on the last two days especially August 16 fall behind the “truth”, which might be attributable to the model’s lack of accuracies in wind fields at high elevations.

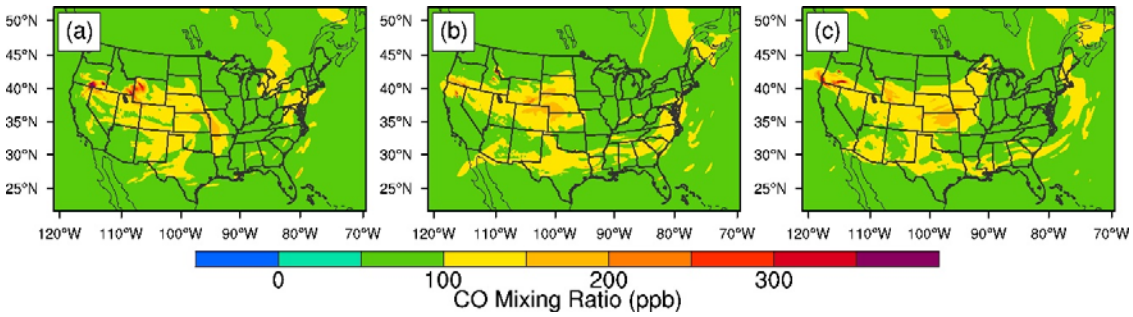

Fig. 3.5: Similar to Fig. 3.4, but with BB emissions five times the default ones.

3.3.2 Effect of the Injection Height

The modeled injection heights in August 2012 were evaluated using MISR observations. For the twenty-three fire plumes examined, Table 3.2 shows that the modeled mean height was 2781 m (AGL) and the observed mean 1867 m (AGL), a nearly 50% overprediction. An overestimation trend was also reported by Val Martin et al. (2012) for the similar plume rise model. But for this study, such a trend might be an artificial effect ascribed to re-gridding multiple fires to the same model grid occasionally. The modeled plume heights were reduced by 50% for another sensitivity test. The results are presented in Fig. 3.6. There are no obvious changes between the base BB case and the sensitivity test except for the Barry Point fire at the borders of California and Oregon. It is not surprising since emissions are squeezed to lower levels with stronger magnitudes.

Table 3.2: Comparison of MISR observed and modeled plume height in August 2012.

Parameter (unit)	MISR plume height	Modeled plume height
Number of samples	23	23
Minimum (m)	838	1329
Maximum (m)	3642	3663
Median (m)	1577	2704
Mean (m)	1846	2729
Standard Deviation (m)	740	528

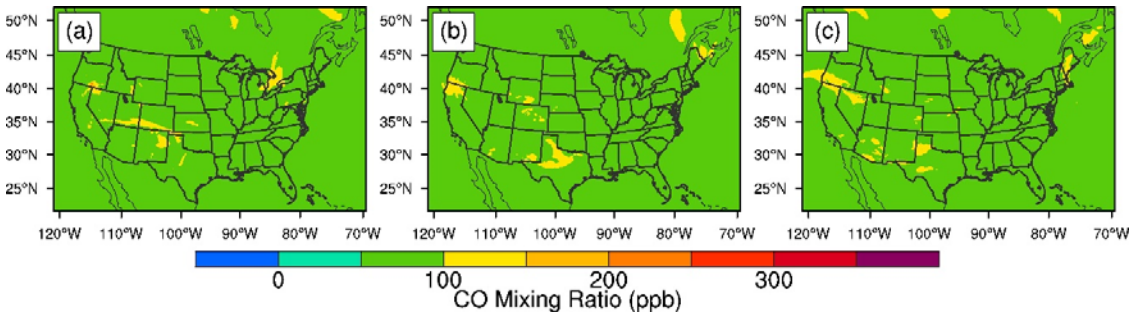

Fig. 3.6: Similar to Fig. 3.4, but the smoke heights were reduced by 50%.

3.3.3 Impacts on Surface Ozone

Fig. 3.7 portrays O_3 changes at the surface layer between the model runs without BB emissions and with five times default BB emissions. On August 14, a belt of O_3 enhancement varied between 5 to 40 ppb is visible along the borders of California, Nevada, Idaho, Utah, and Oregon. Meanwhile, similar O_3 enhancement pervades the downwind state of Wyoming and spreads into Montana and Colorado in less magnitudes. On the following day, the plume propagates southeast reaching the western parts of Nebraska and Kansas with similar O_3 enhancement. On Aug 16, the plume is diluted to enhancements around 15 ppb and hovers the coterminous regions of the states of Colorado, Utah, and Wyoming. Throughout the three days, O_3 enhancements beyond 40 ppb appear in the fire locations in Idaho and North California as well.

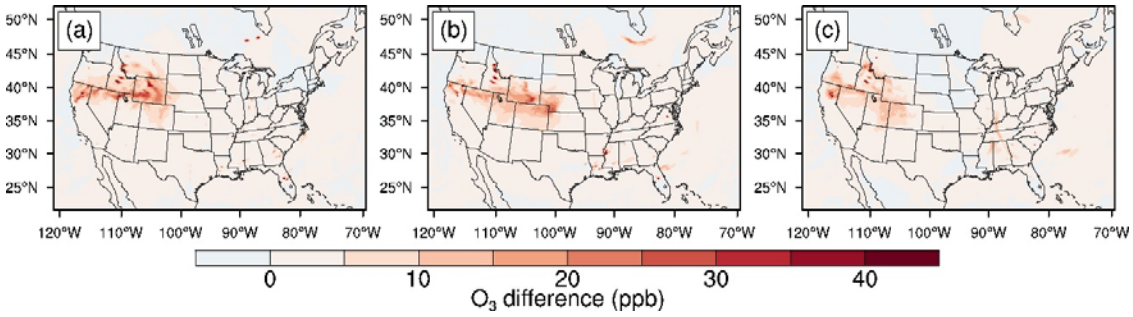

Fig. 3.7: Surface O_3 differences between the simulation without BB emissions and sensitivity run with five times default BB emissions at 20:00 UTC on August 14–16.

3.4 Conclusions

This study applied an offline physical plume rise module to the FINN biomass burning emissions to simulate an intense fire episode in August 2012 in the western U.S. using the CMAQ model. It was found that the base simulation with default FINN emissions underestimated the CO concentrations in the middle of troposphere. Fire plume with peak values about 300 ppb CO were observed moving to the east, which is hardly discernable in the model outputs. The sensitivity run with fire emissions scaled up by a factor of five visually improved the model simulation. Fire plume with modeled 150 ppb or so CO travels to the Great Lakes area in the free troposphere. Comparing to satellite-observed plume height from MISR, the modeled plume height has positive biases. Yet, the sensitivity test reducing plume height by 50% showed little improvement in model-observation comparison for CO. Model results from the sensitivity test with five times default biomass burning emissions indicate that during the fire event more than 40 ppb O_3 were generated near the fire sources at surface and 10 to 30 ppb O_3 enhancements were accumulated along the coterminous borders of California, Nevada, Utah, Colorado, Wyoming, Idaho, and Oregon, which were transported eastward to Kansas and Nebraska and diluted in a couple of days.

Future work will need to confirm the underestimation factor of the FINN emissions by comparing the model results to surface observational data, which will be also necessary to exclude the possible impacts of the vertical mixing from the model. The surface data

will include organic carbon (OC) and black carbon (BC) surface monitoring data from the Interagency Monitoring of Protected Visual Environments (IMRPOVE) network, besides the AQS CO data.

Chapter 4

The contributions of biomass burning to ozone and fine particulate matter ($PM_{2.5}$) in United States in 2012–2014

4.1 Introduction

The impacts of biomass burning on regional air quality are well-known. Fires cause visibility degradation (Levin et al., 2010), property damage, human health problems (Cançado et al., 2006), and casualties. Researchers have found that biomass burning can contribute secondary organic aerosols to haze formation (Huang et al., 2014; Yan et al., 2006), modify cloud properties and precipitation patterns (Lin et al., 2006), or increase tornado severity (Saide et al., 2015). Biomass burning impacts tropospheric chemistry on the local, regional, or even global scales as a major emitter of trace gases and particulate matter (Akagi et al., 2011). Wiedinmyer et al. (2011) estimated that biomass burning released on average 2.0 PgC yr^{-1} globally in 2005–2010, about one fifth of fossil fuel combustion in 2011 (IPCC, 2013). Additionally, biomass burning is responsible for about 40% of the global budget of black carbon (Mao et al., 2011 and references therein), a short-lived climate forcing agent.

Jaffe et al. (2008a; 2008b) estimated that mean $PM_{2.5}$ and O_3 daytime concentrations were enhanced by 1.11 μg m^{-3} and 3.5 ppb, respectively across the western United States during the summer fire seasons of 1988–2004. Elevated aerosol loadings were detected from the surface up to 6 km in the central and southern U.S. when the favorable strong northward wind brought the smoke of the Central American fires in 1998 (Rogers and Bowman 2001; Tanner et al., 2001; Peppler et al., 2000). The adverse effects

of Canadian boreal fires on air quality have been observed in the northern and eastern U.S. and reached as far south as Texas (Morris et al., 2006; DeBell et al., 2004). Analysis of model results signifies the range 10–30 ppb of ozone enhancements originating from a Canadian wildfire (McKeen et al., 2002).

Wildfires are predicted to occur more frequently in a future warmer climate (Daniau et al., 2012). Jacobson et al. (2014) stated that black carbon plays a much bigger role in climate warming and human health than previously thought. U.S. EPA just strengthened the National Ambient Air Quality Standard (NAAQS) for O_3 from 75 ppb to 70 ppb in October 2015. Therefore, it is necessary to quantify the local or even regional impacts of episodic events such as biomass burning on air quality through the contiguous U.S. for future planning. To that end, the Community Multi-scale Air Quality (CMAQ) model was run from April to October in the course of 2012–2014 to determine the contributions of biomass burning to maximum daily 8-hour average (MDA8) surface O_3 and ambient fine particulate matter ($PM_{2.5}$).

4.2 Methodology

4.2.1 Model Description

The 12 km × 12 km grid resolution CMAQ model (Byun and Schere, 2006) version 5.0.2 was employed. Fig. 4.1 shows the model domain with colored land use data. The meteorological inputs were provided by the Advanced Weather Research and Forecasting Model (ARW-WRF) (Skamarock et al., 2008) initialized by the North American Regional Reanalysis (NARR) data (Mesinger et al., 2006). Gas-phase and aerosol chemistries were simulated by the Carbon Band 05 (CB05) mechanism (Yarwood et al., 2005) and the

aerosol module, version 6 (AE6), respectively. Anthropogenic emissions based on the 2011 National Emission Inventory (NEI) were prepared by the Sparse Matrix Operator Kernel Emissions (SMOKE) modeling system. Chemical lateral boundary conditions were interpolated from outputs from GEOS-Chem global chemical transport model (CTM) (Bey et al., 2001). In GEOS-Chem, biomass burning emissions from the Fire Inventory from NCAR (FINN; Wiedinmyer et al., 2011) were distributed uniformly within the boundary layer height. Over the model domain, the FINN version 1.5 provided biomass burning emissions of trace gases and particles. The 1-D cloud-resolving model developed by Freitas et al. (2007) was utilized for distributing fire emissions vertically. Refer to Chapter 3 for the detailed configurations of the model.

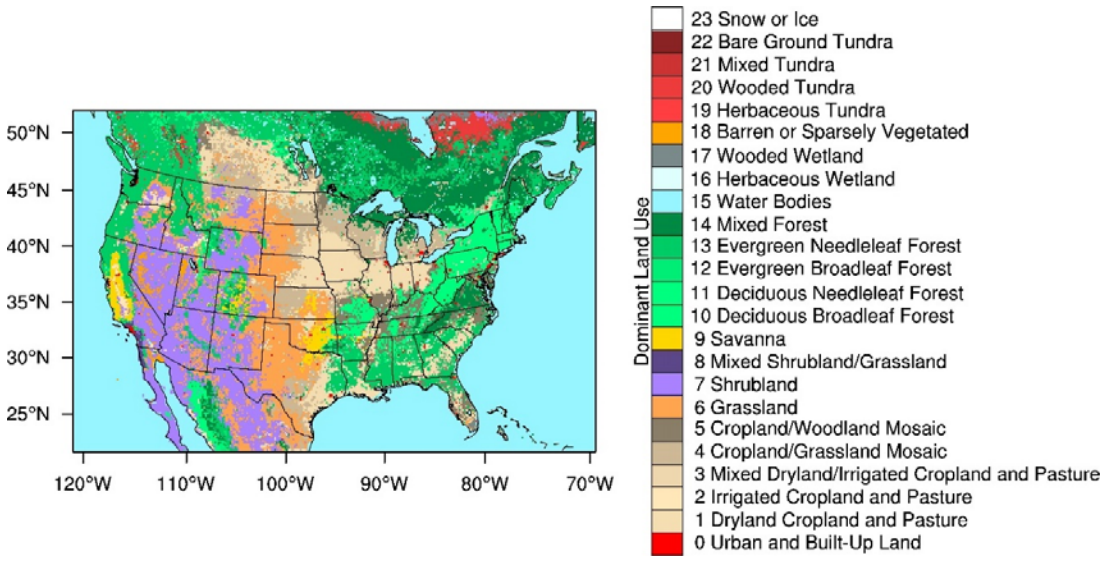

Fig. 4.1: Model domain. Color contour shows dominant land use.

4.2.2 Observations

We relied on hourly surface O_3, CO, and $PM_{2.5}$ concentrations from U.S. EPA's AQS measurement network

(http://aqsdr1.epa.gov/aqsweb/aqstmp/airdata/download_files.html) for model performance evaluations. There are about 1300, 300, and 400 monitoring sites for O_3, CO, and $PM_{2.5}$, respectively. The stations are more concentrated around urban cities. Caution should be exercised in ensuring the validity of the CO observational data.

4.3 Results

4.3.1 Biomass Burning Emissions in 2012–2014

Table 4.1 lists the annual burned area and biomass burning emissions in 2012–2014 in U.S. from FINN v1.5 emission inventory. According to the means of the three years in the bottom row, the year 2012 is an active fire year. During August–September 2012, the highest wild fire activities over the last decade since 2002 in the Western U.S. (McDonald-Buller et al., 2015) burned totally nearly 4,714,372 acres (19,078 km^2) (NOAA, 2012b), about the land area of South Dakota.

Table 4.1: Annual burned area and biomass burning emissions in 2012–2014 in U.S. from FINN v1.5 emission inventory. The unit for burned area is 10^{-3} km^2 and for other species Gg yr^{-1} except for CO_2, which is Tg yr^{-1}. The last row is the mean values for the three years.

	Area	CO_2	CO	NO	NO_2	SO_2	NH_3	CH_4	NMOC	$PM_{2.5}$	OC	BC	PM_{10}	NMHC
2012	44	109	6115	63	187	55	95	259	1601	708	399	36	898	315
2013	33	80	4605	49	138	40	75	198	1195	524	294	27	660	241
2014	35	62	4053	34	114	37	64	183	1026	513	277	20	683	170
Mean	39	87	5045	52	152	44	80	218	1303	587	328	29	753	248

4.3.2 Model Evaluation

Overall, the model simulation with FINN biomass emissions achieved reasonable agreement with observations. The regions that our evaluation will be focused on are depicted in Fig. 4.2. The time was divided into spring (April-May), summer (June-August), and fall (September-October) seasons. The statistics for 2012 are listed in Table 4.2. The statistical metrics for $PM_{2.5}$ are relatively worse probably due to the uncertainties in the

aerosol precursor emissions and the aerosol chemistry in the model. More comprehensive analyses are underway. Refer to Choi et al. (2016) for more details about the model performance.

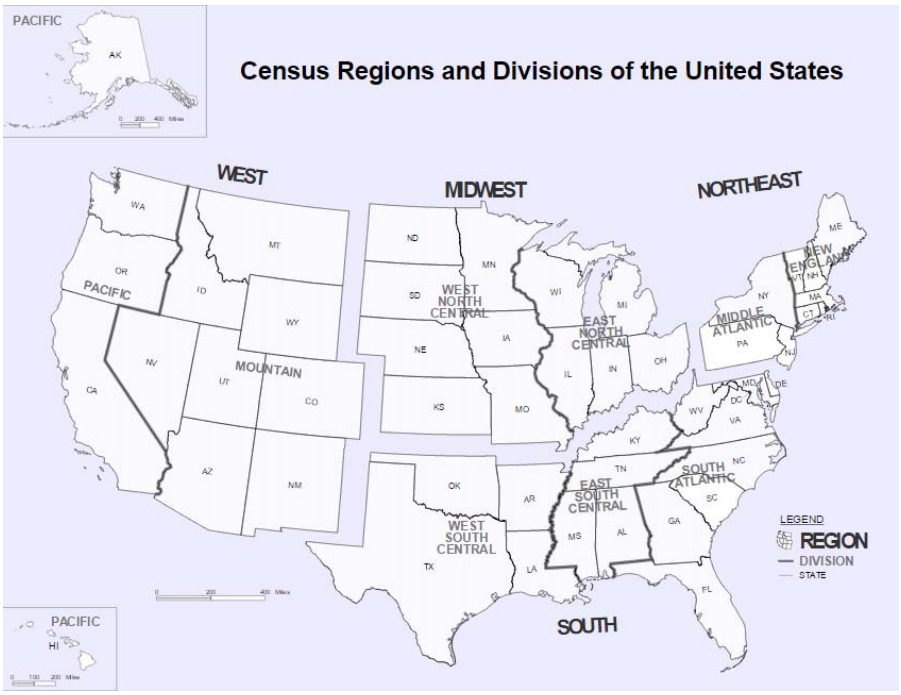

Fig. 4.2: U.S. Census Bureau regions and divisions (http://www2.census.gov/geo/pdfs/maps-data/maps/reference/us_regdiv.pdf)

Table 4.2: Statistical summary of the model evaluations of CO, O_3, and $PM_{2.5}$ for 2012 for the regions in Fig. 4.2. Region 1: Mid-Atlantic; Region 2: Midwest_east_north_central; Region 3: Midwest_west_north_central; Region 4: New England; Region 5: South Atlantic; Region 6: South_east_central; Region 7: South_west_central; Region 8: West_mountain; Region 9: West_Pacific. Corr represents the correlation coefficient; MB mean bias; MAB mean absolute bias; RMSE root-mean-squared error. "-" means statistical number is not available.

	Region 1	Region 2	Region 3	Region 4	Region 5	Region 6	Region 7	Region 8	Region 9
					Spring CO				
Corr	0.54	-	0.48	-	0.66	0.58	0.64	-	0.65
MB (ppb)	-174	-	-61	-	-59	-181	-38	-	-106

MAB (ppb)	175	-	64.2	-	62.3	182	49.9	-	111
RMSE (ppb)	192	-	81.6	-	81.6	192	73.9	-	142
				Spring O_3					
Corr	0.75	0.89	0.83	0.66	0.86	0.91	0.93	0.86	0.87
MB (ppb)	2.52	0.18	0.03	-1.6	4.78	4.93	3.52	-3.2	-0.3
MAB (ppb)	7.19	4.25	4.48	6.87	6.20	5.87	4.70	4.89	4.13
RMSE (ppb)	8.75	5.48	5.51	8.49	7.56	7.38	5.71	6.06	5.89
				Spring $PM_{2.5}$					
Corr	0.58	0.60	0.55	0.63	0.57	0.53	0.29	0.13	0.49
MB ($\mu g\ m^{-3}$)	3.93	1.86	0.7	1.18	-1.5	1.74	-1.6	-2.5	-1.1
MAB ($\mu g\ m^{-3}$)	4.70	3.60	2.86	3.05	2.56	3.87	4.07	3.04	2.32
RMSE ($\mu g\ m^{-3}$)	6.51	4.89	3.94	4.40	3.04	4.94	5.10	4.41	2.83
				Summer CO					
Corr	-	-	0.45	0.62	0.58	-	0.61	-	-
MB (ppb)	-	-	-68	-92	-59	-	-30	-	-
MAB (ppb)	-	-	71.6	93.3	67.5	-	44.1	-	-
RMSE (ppb)	-	-	90	103	83.7	-	65.5	-	-
				Summer O_3					
Corr	0.90	0.94	0.93	0.86	0.94	0.94	0.94	0.92	0.94
MB (ppb)	6.77	1.13	-1.1	5.15	7.30	4.36	4.44	-2.9	-3.5
MAB (ppb)	7.96	4.44	3.75	7.06	7.64	5.61	5.34	3.90	4.17
RMSE (ppb)	9.58	5.44	4.67	8.77	8.52	6.70	6.36	4.83	5.07
				Summer $PM_{2.5}$					
Corr	0.68	0.61	0.55	0.68	0.55	0.61	0.37	0.40	0.22
MB ($\mu g\ m^{-3}$)	2.32	0.0	-1.6	-0.5	-3.0	0.06	-3.2	-3.1	-3.3
MAB ($\mu g\ m^{-3}$)	3.69	2.60	2.66	2.49	3.53	3.07	4.22	3.39	3.50
RMSE ($\mu g\ m^{-3}$)	4.84	3.53	3.53	3.18	4.29	4.02	5.33	4.18	4.06
				Fall CO					
Corr	0.66	0.47	0.61	0.67	0.80	0.58	0.69	0.72	0.67
MB (ppb)	-197	-302	-88	-69	-97	-217	-83	-207	-225

MAB (ppb)	199	302	93.9	73.8	97.7	218	90.0	207	275
RMSE (ppb)	224	318	116	90.0	111	240	135	244	302
				Fall O_3					
Corr	0.87	0.89	0.89	0.76	0.89	0.90	0.92	0.9	0.92
MB (ppb)	5.89	1.62	-1.0	4.46	7.15	4.97	3.21	-0.6	-0.3
MAB (ppb)	6.47	3.99	3.71	6.65	7.41	5.85	4.45	3.38	3.52
RMSE (ppb)	8.58	5.28	4.51	8.58	8.04	7.28	5.65	4.18	4.73
				Fall $PM_{2.5}$					
Corr	0.69	0.73	0.69	0.71	0.63	0.67	0.50	0.39	0.62
MB ($\mu g\ m^{-3}$)	6.35	4.02	2.79	3.50	1.36	4.62	1.56	-2.1	-4.3
MAB ($\mu g\ m^{-3}$)	6.59	4.27	3.41	4.11	2.75	5.10	3.45	3.53	4.49
RMSE ($\mu g\ m^{-3}$)	8.52	5.52	4.51	5.43	3.64	6.22	4.62	4.92	5.57

4.3.3 Biomass Burning Contributions to $PM_{2.5}$

Fig. 4.3 plots average differences of daily $PM_{2.5}$ between simulations with and without biomass burning emissions for each month. During spring (upper row), prescribed fires result in 1–6 $\mu g\ m^{-3}$ mean net daily $PM_{2.5}$ mainly in eastern Kansas (Towne and Craine, 2016) and southeastern U.S. in April, and northern Idaho (Tomback et al., 1995) in May. During summer (middle row), boreal wildfires in northern Canadian (Natural Resources, 2016) produce widespread enhancement of daily $PM_{2.5}$ with more than 20 $\mu g\ m^{-3}$ near source regions. But most smoke is confined within Canada's territory. The effects of intense wildland fires in central Idaho and northern California are prominent in August with peak values exceeding 20 $\mu g\ m^{-3}$. Three large fires, the Mustang Complex, Halstead fire, and Trinity Ridge fire, burned totally 670,268 acres (2,712 km^2) during summer 2012 (NIFC, 2016). The Mustang Complex fire was ignited by lightning on July 30 and was

contained on October 20. The influences of those fires extend as the core region expands and the smoke spread to neighboring states in the next month. The 2012 Whitewater-Baldy fire, the largest wildfire in New Mexico history, is also evident in May–June having peak values 10–12 µg m^{-3}. Some western states such as Oregon and Washington always have occasional fires throughout a year contributing 2 to 20 µg m^{-3} or more mean daily $PM_{2.5}$ near the fire sources. During fall (lower row), the impact of controlled fire emerge repeatedly in the southeast. The contributions of $PM_{2.5}$ reach less than 12 µg m^{-3} mostly in Alabama in October.

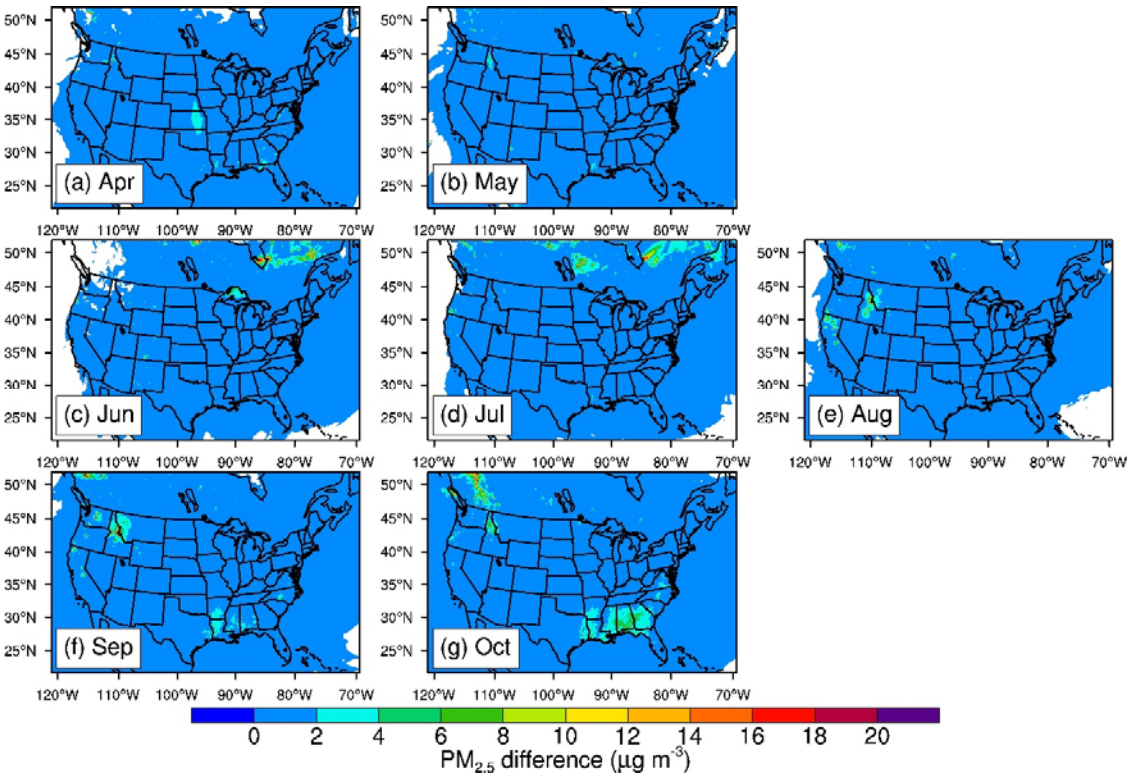

Fig. 4.3: Maps of monthly averaged daily $PM_{2.5}$ difference between simulations with and without biomass burning emissions from 2012 to 2014.

4.3.4 Biomass Burning Contributions to MDA8 O_3

Fig. 4.4 shows the contributions from biomass burning to mean MDA8 O_3 over U.S. The impacts of biomass burning occurred at the location and time consistent with those in Fig. 4.3, for example, prescribed burnings in eastern Kansas in April, northern Idaho in May, and southeastern U.S. in spring and fall. Contributions of the prescribed biomass burning to the mean MDA8 O_3 usually in the range of 1–4 ppb. Wildfires in central Idaho in 2012 are distinct in the months of August and September for their broader and stronger influences. Fire-induced O_3 enhancement pervades most of Idaho with about 9 ppb in the centers of the fires and gradually decreases to about 1 ppb in the areas in neighboring states. Also, impacts of other wildfires such as those in northern California, Oregon, and Washington exhibit local impacts ranging from 1 ppb to 9 ppb to mean MDA8 O_3 mainly during the warm and arid fire seasons (July–September) (Wise, 2012).

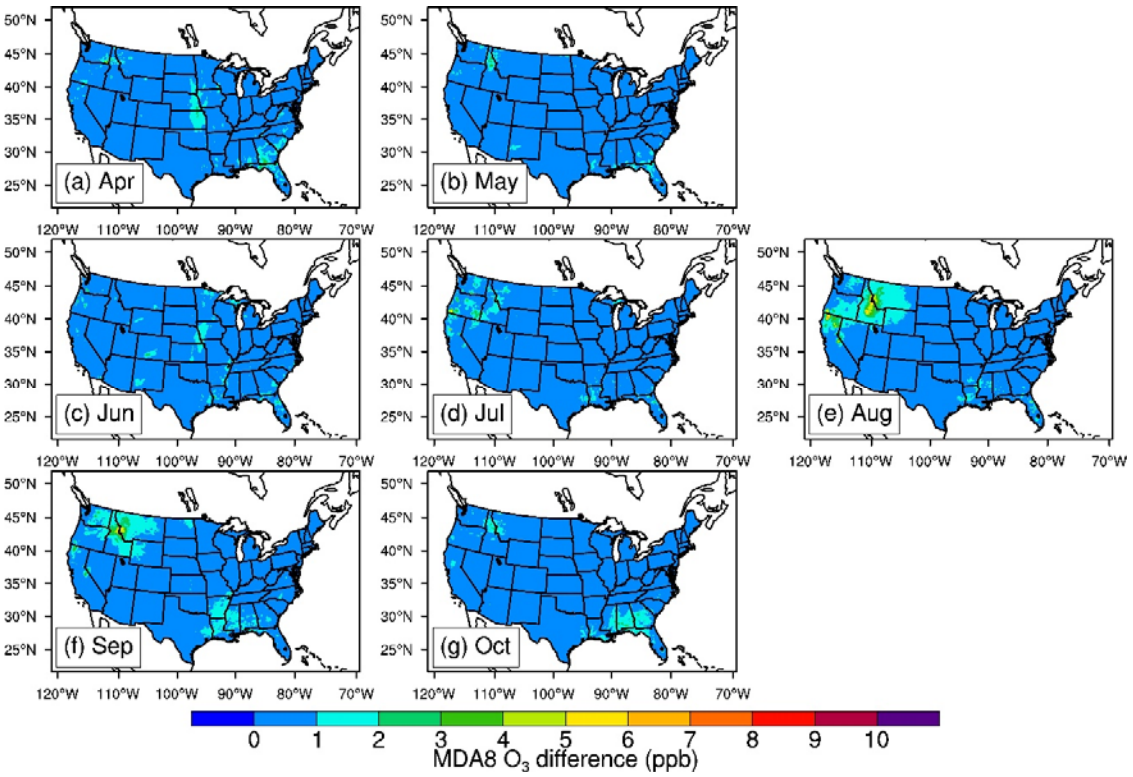

Fig. 4.4: Similar to Fig. 4.3, but for MDA8 O_3.

4.4 Conclusions

In order to quantify the contributions of biomass burning to fine particulate matter ($PM_{2.5}$) and O_3 in U.S., 12 km CMAQ simulations with and without FINN biomass burning emissions have been performed for the months of April to October in 2012–2014. The statistical evaluation shows reasonable agreement between model predictions with biomass burning emissions and ground-based observational data with better performance for O_3 than for $PM_{2.5}$. Model results show that during spring months (April and May) and fall months (September and October), agricultural and prescribed fires lead to 2 to 12 μg m^{-3} $PM_{2.5}$ and 1 to 4 ppb MDA8 O_3 mainly in southeastern U.S., north Idaho and eastern

Kansas, whereas wildfires contribute 2 to 20 μg m^{-3} or more $PM_{2.5}$ and 1–9 ppb MDA8 O_3 throughout the year, particularly in the summer–fall fire seasons in western U.S. The strongest wildfire impacts were limited to the remote fire-origin regions.

References

Akagi, S. K., R. J. Yokelson, C. Wiedinmyer, M. J. Alvarado, J. S. Reid, T. Karl, J. D. Crounse, and P. O. Wennberg. 2011. Emission factors for open and domestic biomass burning for use in atmospheric models. *Atmos. Chem. Phys.* 11 (9):4039–4072.

Al-Saadi, J., A. J. Soja, R. B. Pierce, J. Szykman, C. Wiedinmyer, L. Emmons, S. Kondragunta, X. Zhang, C. Kittaka, T. Schaack, and K. Bowman. 2008. Intercomparison of near-real-time biomass burning emissions estimates constrained by satellite fire data. *J. Appl. Remote Sens.* 2 (1):021504-021504-24.

Alicke, B., A. Geyer, A. Hofzumahaus, F. Holland, S. Konrad, H. W. Pätz, J. Schäfer, J. Stutz, A. Volz-Thomas, and U. Platt. 2003. OH formation by HONO photolysis during the BERLIOZ experiment. *J. Geophys. Res.-Atmos.* 108 (D4):8247.

Alicke, B., U. Platt, and J. Stutz. 2002. Impact of nitrous acid photolysis on the total hydroxyl radical budget during the Limitation of Oxidant Production/Pianura Padana Produzione di Ozono study in Milan. *J. Geophys. Res.-Atmos.* 107 (D22):LOP 9-1-LOP 9-17.

Andela, N., J. W. Kaiser, G. R. van der Werf, and M. J. Wooster. 2015. New fire diurnal cycle characterizations to improve fire radiative energy assessments made from MODIS observations. *Atmos. Chem. Phys.* 15 (15):8831–8846.

Andreae, M. O., and P. Merlet. 2001. Emission of trace gases and aerosols from biomass burning. *Global Biogeochem. Cy.* 15 (4):955–966.

Apel, E. C., D. D. Riemer, A. Hills, W. Baugh, J. Orlando, I. Faloona, D. Tan, W. Brune, B. Lamb, H. Westberg, M. A. Carroll, T. Thornberry, and C. D. Geron. 2002. Measurement and interpretation of isoprene fluxes and isoprene, methacrolein, and methyl vinyl ketone mixing ratios at the PROPHET site during the 1998 Intensive. *J. Geophys. Res.-Atmos.* 107 (D3).

Atkinson, R. 2000. Atmospheric chemistry of VOCs and NOx. *Atmos. Environ.* 34 (12–14):2063–2101.

Ayres, B. R., H. M. Allen, D. C. Draper, S. S. Brown, R. J. Wild, J. L. Jimenez, D. A. Day, P. Campuzano-Jost, W. Hu, J. de Gouw, A. Koss, R. C. Cohen, K. C. Duffey, P. Romer, K. Baumann, E. Edgerton, S. Takahama, J. A. Thornton, B. H. Lee, F. D. Lopez-Hilfiker, C. Mohr, P. O. Wennberg, T. B. Nguyen, A. Teng, A. H. Goldstein, K. Olson, and J. L. Fry. 2015. Organic nitrate aerosol formation via NO_3 + biogenic volatile organic compounds in the southeastern United States. *Atmos. Chem. Phys.* 15 (23):13377–13392.

Bey, I., D. J. Jacob, R. M. Yantosca, J. A. Logan, B. D. Field, A. M. Fiore, Q. Li, H. Y. Liu, L. J. Mickley, and M. G. Schultz. 2001. Global modeling of tropospheric chemistry with assimilated meteorology: Model description and evaluation. *J. Geophys. Res-Atmos.* 106 (D19):23073–23095.

Borbon, A., H. Fontaine, M. Veillerot, N. Locoge, J. C. Galloo, and R. Guillermo. 2001. An investigation into the traffic-related fraction of isoprene at an urban location. *Atmos. Environ.* 35 (22):3749–3760.

Briggs, G. A. 1975. Plume rise predictions, in *Lectures on Air Pollution and Environmental Impact Analyses,* edited by Haugen, D., pp. 72–73. American Meteorological Society, Boston, MA, United States.

Brown, S. S., J. A. deGouw, C. Warneke, T. B. Ryerson, W. P. Dubé, E. Atlas, R. J. Weber, R. E. Peltier, J. A. Neuman, J. M. Roberts, A. Swanson, F. Flocke, S. A. McKeen, J. Brioude, R. Sommariva, M. Trainer, F. C. Fehsenfeld, and A. R. Ravishankara. 2009. Nocturnal isoprene oxidation over the Northeast United States in summer and its impact on reactive nitrogen partitioning and secondary organic aerosol. *Atmos. Chem. Phys.* 9 (9):3027–3042.

Brown, S. S., W. P. Dubé, H. D. Osthoff, D. E. Wolfe, W. M. Angevine, and A. R. Ravishankara. 2007. High resolution vertical distributions of NO_3 and N_2O_5 through the nocturnal boundary layer. *Atmos. Chemis. Phys.* 7:139–149.

Brown, S. S., W. P. Dubé, J. Peischl, T. B. Ryerson, E. Atlas, C. Warneke, J. A. de Gouw, S. t. L.. Hekkert, C. A. Brock, F. Flocke, M. Trainer, D. D. Parrish, F. C. Feshenfeld, and A. R. Ravishankara. 2011. Budgets for nocturnal VOC oxidation by nitrate radicals aloft during the 2006 Texas Air Quality Study. *J. Geophys. Res.-Atmos.* 116.

Burkholder, J. B., S. P. Sander, J. Abbatt, J. R. Barker, R. E. Huie, C. E. Kolb, M. J. Kurylo, V. L. Orkin, D. M. Wilmouth, and P. H. Wine. 2015. Chemical Kinetics and Photochemical Data for Use in Atmospheric Studies, Evaluation NO. 18. JPL Publication 15–10, Jet Propulsion Laboratory, Pasadena, California, U.S.A. http://jpldataeval.jpl.nasa.gov (Accessed December 23, 2016).

Buszewski, B., M. Kesy, T. Ligor, and A. Amann. 2007. Human exhaled air analytics: Biomarkers of diseases. *Biomed. Chromatogr.* 21 (6):553–566.

Byun, D., and K. L. Schere. 2006. Review of the governing equations, computational algorithms, and other components of the models-3 Community Multiscale Air Quality (CMAQ) modeling system. *Appl. Mech. Rev.* 59 (2):51–77.

Calvert, J. G., G. Yarwood, and A. M. Dunker. 1994. An evaluation of the mechanism of nitrous acid formation in the urban atmosphere. *Res. Chem. Intermed.* 20 (3–5):463–502.

Cançado, J. E.D., P. H. N. Saldiva, A. A. P. Luiz, L. B. L. S. Lara, P. Artaxo, L. A. Martinelli, M. A. Arbex, A. Zanobetti, and L. F. B. Alfesio. 2006. The impact of sugar cane-burning emissions on the respiratory system of children and the elderly. *Environ. Health Persp.* 114 (5):725–729.

Carroll, M., J. Townshend, M. Hansen, C. DiMiceli, R. Sohlberg, and K. Wurster. 2011. MODIS vegetative cover conversion and vegetation continuous fields, in *Land Remote Sensing and Global Environmental Change*, edited by B. Ramachandran, C. O. Justice and M. J. Abrams, pp. 725–745. Springer, New Jork.

Chang, C.-C., J.-L. Wang, S.-C. C. Lung, C.-Y. Chang, P.-J. Lee, C. Chew, W.-C. Liao, W.-N. Chen, and C.-F. O.-Yang. 2014. Seasonal characteristics of biogenic and anthropogenic isoprene in tropical-subtropical urban environments. *Atmos. Environ.* 99:298–308.

Chauvel, A., and G. Lefebvre. 1989. *Petrochemical Processes: Synthesis-gas Derivatives and Major Hydrocarbons*. Editions Technip, Parish.

Chen, Y., Q. Li, J. T. Randerson, E. A. Lyons, R. A. Kahn, D. L. Nelson, and D. J. Diner. 2009. The sensitivity of CO and aerosol transport to the temporal and vertical distribution of North American boreal fire emissions. *Atmos. Chem. Phys.* 9 (17):6559–6580.

Choi, Y., W. Jeon, A. Roy, A. H. Souri, L. Diao, S. Pan, and Eslami E. 2016. CMAQ modeling archive for exceptional events analyses. The Texas Commission on Environmental Quality, Austin, Texas. https://www.tceq.texas.gov/assets/public/implementation/air/am/contracts/reports/pm/5821554181FY1609-20160829-uh-CMAQModelingArchiveForExceptionalEventsAnalyses.pdf (Accessed November 7, 2016)

Choi, Y., G. Osterman, A. Eldering, Y. Wang, and E. Edgerton. 2010. Understanding the contributions of anthropogenic and biogenic sources to CO enhancements and outflow observed over North America and the western Atlantic Ocean by TES and MOPITT. *Atmos. Environ.* 44 (16):2033–2042.

Choi, Y., and A. H. Souri. 2015. Chemical condition and surface ozone in large cities of Texas during the last decade: Observational evidence from OMI, CAMS, and model analysis. *Remote Sens. Environ.* 168:90–101.

Claeys, M., B. Graham, G. Vas, W. Wang, R. Vermeylen, V. Pashynska, J. Cafmeyer, P. Guyon, M. O. Andreae, P. Artaxo, and W. Maenhaut. 2004. Formation of secondary organic aerosols through photooxidation of isoprene. *Science* 303 (5661):1173–1176.

Czader, B. H., Y. Choi, X. Li, S. Alvarez, and B. Lefer. 2015. Impact of updated traffic emissions on HONO mixing ratios simulated for urban site in Houston, Texas. *Atmos. Chem. Phys.* 15 (3):1253–1263.

Czader, B. H., X. Li, and B. Rappenglück. 2013. CMAQ modeling and analysis of radicals, radical precursors, and chemical transformations. *J.Geophys. Res.-Atmos.* 118 (19):11,376–11,387.

Czader, B. H., B. Rappenglück, P. Percell, D. W. Byun, F. Ngan, and S. Kim. 2012. Modeling nitrous acid and its impact on ozone and hydroxyl radical during the Texas Air Quality Study 2006. *Atmos. Chem. Phys.* 12 (15):6939–6951.

Daniau, A. L., P. J. Bartlein, S. P. Harrison, I. C. Prentice, S. Brewer, P. Friedlingstein, T. I. Harrison-Prentice, J. Inoue, K. Izumi, J. R. Marlon, S. Mooney, M. J. Power, J. Stevenson, W. Tinner, M. Andric, J. Atanassova, H. Behling, M. Black, O. Blarquez, K. J. Brown, C. Carcaillet, E. A. Colhoun, D. Colombaroli, B. A. S. Davis, D. D'Costa, J. Dodson, L. Dupont, Z. Eshetu, D. G. Gavin, A. Genries, S. Haberle, D. J. Hallett, G. Hope, S. P. Horn, T. G. Kassa, F. Katamura, L. M. Kennedy, P. Kershaw, S. Krivonogov, C. Long, D. Magri, E. Marinova, G. M. McKenzie, P. I. Moreno, P. Moss, F. H. Neumann, E. Norstrom, C. Paitre, D. Rius, N. Roberts, G. S. Robinson, N. Sasaki, L. Scott, H. Takahara, V. Terwilliger, F. Thevenon, R. Turner, V. G. Valsecchi, B. Vanniere, M. Walsh, N. Williams, and Y. Zhang. 2012. Predictability of biomass burning in response to climate changes. *Global Biogeochem. Cy.* 26.

DeBell, L. J., R. W. Talbot, J. E. Dibb, J. W. Munger, E. V. Fischer, and S. E. Frolking. 2004. A major regional air pollution event in the northeastern United States caused by extensive forest fires in Quebec, Canada. *J. Geophys. Res-Atmos.* 109 (D19).

Diao, L., Y. Choi, B. Czader, X. Li, S. Pan, A. Roy, A. H. Souri, M. Estes, and W. Jeon. 2016a. Discrepancies between modeled and observed nocturnal isoprene in an urban environment and the possible causes: A case study in Houston. *Atmos. Res.* 181:257–264.

Diao, L., A. Roy, B. Czader, S. Pan, W. Jeon, A. H. Souri, and Y. Choi. 2016b. Modeling the effect of relative humidity on nitrous acid formation in the Houston area. *Atmos. Environ.* 131:78–82.

Emmons, L. K., S. Walters, P. G. Hess, J. F. Lamarque, G. G. Pfister, D. Fillmore, C. Granier, A. Guenther, D. Kinnison, T. Laepple, J. Orlando, X. Tie, G. Tyndall, C. Wiedinmyer, S. L. Baughcum, and S. Kloster. 2010. Description and evaluation of the Model for Ozone and Related chemical Tracers, version 4 (MOZART-4). *Geosci. Model Dev.* 3 (1):43–67.

Field, R. D., M. Lou, M. Fromm, A. Voulgarakis, S. Mangeon, and J. Worden. 2016. Simulating the Black Saturday 2009 smoke plume with an interactive composition-climate model: Sensitivity to emissions amount, timing, and injection height. *J. Geophys. Res.-Atmos.* 121 (8):4296–4316.

Finlayson-Pitts, B. J., L. M. Wingen, A. L. Sumner, D. Syomin, and K. A. Ramazan. 2003. The heterogeneous hydrolysis of NO_2 in laboratory systems and in outdoor and indoor atmospheres: An integrated mechanism. *Phys. Chem. Chem. Phys.* 5 (2):223–242.

Foley, K. M., S. J. Roselle, K. W. Appel, P. V. Bhave, J. E. Pleim, T. L. Otte, R. Mathur, G. Sarwar, J. O. Young, R. C. Gilliam, C. G. Nolte, J. T. Kelly, A. B. Gilliland, and J. O. Bash. 2010.

Incremental testing of the Community Multiscale Air Quality (CMAQ) modeling system version 4.7. *Geosci. Model Dev.* 3 (1):205–226.

Freitas, S. R., K. M. Longo, R. Chatfield, D. Latham, M. A. F. Silva Dias, M. O. Andreae, E. Prins, J. C. Santos, R. Gielow, and J. A. Carvalho Jr. 2007. Including the sub-grid scale plume rise of vegetation fires in low resolution atmospheric transport models. *Atmos. Chem. Phys.* 7 (13):3385–3398.

Freitas, S. R., K. M. Longo, J. Trentmann, and D. Latham. 2010. Technical Note: Sensitivity of 1-D smoke plume rise models to the inclusion of environmental wind drag. *Atmos. Chem. Phys.* 10 (2):585–594.

Friedl, M. A., D. Sulla-Menashe, B. Tan, A. Schneider, N. Ramankutty, A. Sibley, and X. Huang. 2010. MODIS Collection 5 global land cover: Algorithm refinements and characterization of new datasets. *Remote Sens. Enviro.* 114 (1):168–182.

Fu, J. S., N. C. Hsu, Y. Gao, K. Huang, C. Li, N. H. Lin, and S. C. Tsay. 2012. Evaluating the influences of biomass burning during 2006 BASE-ASIA: a regional chemical transport modeling. *Atmos. Chem. Phys.* 12 (9):3837–3855.

Fujita, E. M., D. E. Campbell, B. Zielinska, J. C. Chow, C. E. Lindhjem, A. DenBleyker, G. A. Bishop, B. G. Schuchmann, D. H. Stedman, and D. R. Lawson. 2012. Comparison of the MOVES2010a, MOBILE6.2, and EMFAC2007 mobile source emission models with on-road traffic tunnel and remote sensing measurements. *J. Air Waste Manage.* 62 (10): 1134–1149.

Gantt, B., N. Meskhidze, Y. Zhang, and J. Xu. 2010. The effect of marine isoprene emissions on secondary organic aerosol and ozone formation in the coastal United States. *Atmos. Environ.* 44 (1):115–121.

Giglio, L. 2007. Characterization of the tropical diurnal fire cycle using VIRS and MODIS observations. *Remote Sens. Environ.* 108 (4):407–421.

Giglio, L., I. Csiszar, and C. O. Justice. 2006. Global distribution and seasonality of active fires as observed with the Terra and Aqua Moderate Resolution Imaging Spectroradiometer (MODIS) sensors. *J. Geophys. Res.-Biogeo.* 111 (G2).

Gonzi, S., and P. I. Palmer. 2010. Vertical transport of surface fire emissions observed from space. *J. Geophys. Res.-Atmos.* 115.

Gonçalves, M., D. Dabdub, W. L. Chang, O. Jorba, and J. M. Baldasano. 2012. Impact of HONO sources on the performance of mesoscale air quality models. *Atmos. Environ.* 54:168–176.

Guenther, A., C. N. Hewitt, D. Erickson, R. Fall, C. Geron, T. Graedel, P. Harley, L. Klinger, M. Lerdau, W. A. McKay, T. Pierce, B. Scholes, R. Steinbrecher, R. Tallamraju, J. Taylor, and P. Zimmerman. 1995. A global model of natural volatile organic compound emissions. *J. Geophys. Res.-Atmos.* 100 (D5):8873–8892.

Guenther, A. B., X. Jiang, C. L. Heald, T. Sakulyanontvittaya, T. Duhl, L. K. Emmons, and X. Wang. 2012. The Model of Emissions of Gases and Aerosols from Nature version 2.1 (MEGAN2.1): An extended and updated framework for modeling biogenic emissions. *Geosci. Model Dev.* 5 (6):1471–1492.

Hansen, M. C., R. S. DeFries, J. R. G. Townshend, M. Carroll, C. Dimiceli, and R. A. Sohlberg. 2003. Global percent tree cover at a spatial resolution of 500 meters: First results of the MODIS vegetation continuous fields algorithm. *Earth Interactions* 7.

Hansen, M. C., J. R. G. Townshend, R. S. Defries, and M. Carroll. 2005. Estimation of tree cover using MODIS data at global, continental and regional/local scales. *Int. J. Remote Sens.* 26 (19):4359–4380.

Hao, N., B. Zhou, D. Chen, and L. Chen. 2006. Observations of nitrous acid and its relative humidity dependence in Shanghai. *J. Environ. Sci.* 18 (5):910–915.

Harris, G. W., W. P. L. Carter, A. M. Winer, J. N. Pitts, U. Platt, and D. Perner. 1982. Observations of nitrous acid in the Los Angeles atmosphere and implications for predictions of ozone-precursor relationships. *Environ. Sci. Technol.* 16 (7):414–419.

Heland, J., J. Kleffmann, R. Kurtenbach, and P. Wiesen. 2001. A new instrument to measure gaseous nitrous acid (HONO) in the atmosphere. *Environ. Sci. Technol.* 35 (15):3207–3212.

Horowitz, L. W., A. M. Fiore, G. P. Milly, R. C. Cohen, A. Perring, P. J. Wooldridge, P. G. Hess, L. K. Emmons, and J. Lamarque. 2007. Observational constraints on the chemistry of isoprene nitrates over the eastern United States. *J. Geophys. Res.-Atmos.* 112 (D12):D12S08.

Hu, L., D. B. Millet, M. Baasandorj, T. J. Griffis, P. Turner, D. Helmig, A. J. Curtis, and J. Hueber. 2015. Isoprene emissions and impacts over an ecological transition region in the US Upper Midwest inferred from tall tower measurements. *J. Geophys. Res.-Atmos.* 120 (8):3553–3571.

Huang, R.-J., Y. Zhang, C. Bozzetti, K.-F. Ho, J.-J. Cao, Y. Han, K. R. Daellenbach, J. G. Slowik, S. M. Platt, F. Canonaco, P. Zotter, R. Wolf, S. M. Pieber, E. A. Bruns, M. Crippa, G. Ciarelli, A. Piazzalunga, M. Schwikowski, G. Abbaszade, J. Schnelle-Kreis, R. Zimmermann, Z. An, S. Szidat, U. Baltensperger, I. E. Haddad, and A. S. H. Prevot. 2014. High secondary aerosol contribution to particulate pollution during haze events in China. *Nature* 514 (7521):218–222.

HYSPLIT, 2015. Air Resources Laboratory, http://ready.arl.noaa.gov/HYSPLIT.php

In, H., D. W. Byun, R. J. Park, N. Moon, S. Kim, and S. Zhong. 2007. Impact of transboundary transport of carbonaceous aerosols on the regional air quality in the United States: A case study of the South American wildland fire of May 1998. *J. Geophys. Res.-Atmos.* 112 (D7).

IPCC, 2013: Climate Change 2013. The Physical Science Basis. Contribution of Working Group I to the Fifth Assessment Report of the Intergovernmental Panel on Climate Change. ed. Stocker, T.F., D. Qin, G.-K. Plattner, M. Tignor, S.K. Allen, J. Boschung, A. Nauels, Y. Xia, V. Bex, P.M. Midgley. Cambridge University Press, United Kingdom and New York, NY, USA, 1535 pp.

Jacob, D. J. 2000. Heterogeneous chemistry and tropospheric ozone. *Atmos. Environ.* 34 (12–14):2131–2159.

Jacobson, M. Z. 2005. *Fundamentals of Atmospheric Modeling*. 2nd ed. Cambridge University Press, New York, U.S.A.

Jacobson, M. Z. 2014. Effects of biomass burning on climate, accounting for heat and moisture fluxes, black and brown carbon, and cloud absorption effects. *J. Geophys. Res.-Atmos.* 119 (14):8980–9002.

Jaffe, D., I. Bertschi, L. Jaeglé, P. Novelli, J. S. Reid, H. Tanimoto, R. Vingarzan, and D. L. Westphal. 2004. Long-range transport of Siberian biomass burning emissions and impact on surface ozone in western North America. *Geophys. Res. Lett.* 31 (16): L16106.

Jaffe, D., D. Chand, W. Hafner, A. Westerling, and D. Spracklen. 2008a. Influence of fires on O_3 concentrations in the western US. *Environ. Sci. Technol.* 42 (16):5885–5891.

Jaffe, D., W. Hafner, D. Chand, A. Westerling, and D. Spracklen. 2008b. Interannual variations in PM2.5 due to wildfires in the Western United States. *Environ. Sci. Technol.* 42 (8):2812–2818.

Jenkin, M. E., R. A. Cox, and D. J. Williams. 1988. Laboratory studies of the kinetics of formation of nitrous acid from the thermal reaction of nitrogen dioxide and water vapour. *Atmos. Environ.* (1967) 22 (3):487–498.

Kahn, R. A., Y. Chen, D. L. Nelson, F.-Y. Leung, Q. Li, D. J. Diner, and J. A. Logan. 2008. Wildfire smoke injection heights: Two perspectives from space. *Geophys. Res. Lett.* 35 (4):L04809.

Karamchandani, P., C. Emery, G. Yarwood, B. Lefer, J. Stutz, E. Couzo, and W. Vizuete. 2015. Implementation and refinement of a surface model for heterogeneous HONO formation in a 3-D chemical transport model. *Atmos. Environ.* 112:356–368.

Khan, M. A. H., M. C. Cooke, S. R. Utembe, A. T. Archibald, R. G. Derwent, P. Xiao, C. J. Percival, M. E. Jenkin, W. C. Morris, and D. E. Shallcross. 2015. Global modeling of the nitrate radical (NO_3) for present and pre-industrial scenarios. *Atmos. Res.* 164–165:347–357.

Kleffmann, J. 2007. Daytime sources of nitrous acid (HONO) in the atmospheric boundary layer. *ChemPhysChem* 8 (8):1137–1144.

Kleffmann, J., K. H. Becker, and P. Wiesen. 1998. Heterogeneous NO_2 conversion processes on acid surfaces: Possible atmospheric implications. *Atmos. Environ.* 32 (16):2721–2729.

Kleffmann, J., T. Gavriloaiei, A. Hofzumahaus, F. Holland, R. Koppmann, L. Rupp, E. Schlosser, M. Siese, and A. Wahner. 2005. Daytime formation of nitrous acid: A major source of OH radicals in a forest. *Geophys. Res. Lett.* 32 (5):L05818.

Kleinman, L. I., P. H. Daum, D. Imre, Y. N. Lee, L. J. Nunnermacker, S. R. Springston, J. Weinstein-Lloyd, and J. Rudolph. 2002. Ozone production rate and hydrocarbon reactivity in 5 urban areas: A cause of high ozone concentration in Houston. *Geophys. Res. Lett.* 29 (10):105-1-105-4.

Kroll, J. H., N. L. Ng, S. M. Murphy, R. C. Flagan, and J. H. Seinfeld. 2006. Secondary organic aerosol formation from isoprene photooxidation. *Environ. Sci.Technol.* 40 (6):1869–1877.

Kurtenbach, R., K. H. Becker, J. A. G. Gomes, J. Kleffmann, J. C. Lörzer, M. Spittler, P. Wiesen, R. Ackermann, A. Geyer, and U. Platt. 2001. Investigations of emissions and heterogeneous formation of HONO in a road traffic tunnel. *Atmos. Environ.* 35 (20):3385–3394.

Lammel, G., and J. N. Cape. 1996. Nitrous acid and nitrite in the atmosphere. *Chem. Soc. Rev.* 25 (5):361–369.

Lamsal, L. N., R. V. Martin, A. van Donkelaar, M. Steinbacher, E. A. Celarier, E. Bucsela, E. J. Dunlea, and J. P. Pinto. 2008. Ground-level nitrogen dioxide concentrations inferred from the satellite-borne Ozone Monitoring Instrument. *J. Geophys. Res.-Atmos.* 113 (D16).

Leuchner, M., and B. Rappenglück. 2010. VOC source-receptor relationships in Houston during TexAQS-II. *Atmos. Environ.* 44 (33):4056–4067.

Leung, F.-Y. T., J. A. Logan, R. Park, E. Hyer, E. Kasischke, D. Streets, and L. Yurganov. 2007. Impacts of enhanced biomass burning in the boreal forests in 1998 on tropospheric chemistry and the sensitivity of model results to the injection height of emissions. *J. Geophys. Res-Atmos.* 112 (D10):D10313.

Levin, E. J. T., G. R. McMeeking, C. M. Carrico, L. E. Mack, S. M. Kreidenweis, C. E. Wold, H. Moosmüller, W. P. Arnott, W. M. Hao, J. L. Collett, and W. C. Malm. 2010. Biomass burning smoke aerosol properties measured during Fire Laboratory at Missoula Experiments (FLAME). *J. Geophys. Res.-Atmos.* 115 (D18): D18210.

Li, X., T. Brauers, R. Häseler, B. Bohn, H. Fuchs, A. Hofzumahaus, F. Holland, S. Lou, K. D. Lu, F. Rohrer, M. Hu, L. M. Zeng, Y. H. Zhang, R. M. Garland, H. Su, A. Nowak, A. Wiedensohler, N. Takegawa, M. Shao, and A. Wahner. 2012. Exploring the atmospheric chemistry of nitrous acid (HONO) at a rural site in Southern China. *Atmos. Chem. Phys.* 12 (3):1497–1513.

Li, X., Y. Choi, B. Czader, A. Roy, H. Kim, B. Lefer, and S. Pan. 2016. The impact of observation nudging on simulated meteorology and ozone concentrations during DISCOVER-AQ 2013 Texas campaign. *Atmos. Chem. Phys.* 16 (5):3127–3144.

Li, S., J. Matthews, and A. Sinha. 2008. Atmospheric hydroxyl radical production from electronically excited NO_2 and H_2O. *Science* 319 (5870):1657–1660.

Li, G., R. Zhang, J. Fan, and X. Tie. 2007. Impacts of biogenic emissions on photochemical ozone production in Houston, Texas. *J. Geophys. Res.-Atmos.* 112 (D10):D10309.

Liakakou, E., M. Vrekoussis, B. Bonsang, Ch Donousis, M. Kanakidou, and N. Mihalopoulos. 2007. Isoprene above the Eastern Mediterranean: Seasonal variation and contribution to the oxidation capacity of the atmosphere. *Atmos. Environ.* 41 (5):1002–1010.

Lin, J. C., T. Matsui, R. A. Pielke, Sr., and C. Kummerow. 2006. Effects of biomass-burning-derived aerosols on precipitation and clouds in the Amazon Basin: a satellite-based empirical study. *J. Geophys. Res.-Atmos.* 111 (D19).

Main, H. H., T. O'Brien, C. Hardy, S. Wharton, and D. Sullivan. 2001. Characterization of AUTO-GC data in Houston. Extended Outline STI-900610-2112-EO, Texas Natural Resource Conservation Commission, Austin, Texas, U.S.A. https://www.tceq.texas.gov/assets/public/implementation/air/am/contracts/reports/da/CharacterizationAutoGCdata.pdf (Accessed April 5, 2016).

Mao, Y. H., Q. B. Li, L. Zhang, Y. Chen, J. T. Randerson, D. Chen, and K. N. Liou. 2011. Biomass burning contribution to black carbon in the Western United States Mountain Ranges. *Atmos. Chem. Phys.* 11 (21):11253–11266.

Mao, J., F. Paulot, D. J. Jacob, R. C. Cohen, J. D. Crounse, P. O. Wennberg, C. A. Keller, R. C. Hudman, M. P. Barkley, and L. W. Horowitz. 2013. Ozone and organic nitrates over the eastern United States: Sensitivity to isoprene chemistry. *J. Geophys. Res.-Atmos.* 118 (19):11,256–11,268.

Matsunaga, S., M. Mochida, T. Saito, and K. Kawamura. 2002. In situ measurement of isoprene in the marine air and surface seawater from the western North Pacific. *Atmos. Environ.* 36 (39–40):6051–6057.

McDonald-Buller, E., Y. Kimura, C. Wiedinmyer, C. Emery, Z. Liu, G. Yarwood, and R. Environ. 2015. Targeted improvements in the Fire INventory from NCAR (FINN) Model for Texas air quality planning. The University of Texas at Austin, Austin, Texas, U.S.A. http://aqrp.ceer.utexas.edu/projectinfoFY14_15%5C14-011%5C14-011%20Final%20Report.pdf (Accessed November 6, 2016)

McKeen, S. A., G. Wotawa, D. D. Parrish, J. S. Holloway, M. P. Buhr, G. Hübler, F. C. Fehsenfeld, and J. F. Meagher. 2002. Ozone production from Canadian wildfires during June and July of 1995. *J. Geophys. Res.-Atmos.* 107 (D14):ACH 7-1-ACH 7–25.

McLaren, R., D. L. Singleton, J. Y. K. Lai, B. Khouw, E. Singer, Z. Wu, and H. Niki. 1996. Analysis of motor vehicle sources and their contribution to ambient hydrocarbon distributions at urban sites in Toronto during the Southern Ontario oxidants study. *Atmos. Environ.* 30 (12):2219–2232.

McMillan, W. W., C. Barnet, L. Strow, M. T. Chahine, M. L. McCourt, J. X. Warner, P. C. Novelli, S. Korontzi, E. S. Maddy, and S. Datta. 2005. Daily global maps of carbon monoxide from NASA's Atmospheric Infrared Sounder. *Geophys. Res. Lett.* 32 (11): L11801.

Melillo, J. M., T.C. Richmond, and G. W. Yohe, Eds., 2014. Highlights of climate change impacts in the United States: The Third National Climate Assessment. U.S. Global Change Research Program., 841 pp.

Mesinger, F., G. DiMego, E. Kalnay, K. Mitchell, P. C. Shafran, W. Ebisuzaki, D. Jović, J. Woollen, E. Rogers, E. H. Berbery, M. B. Ek, Y. Fan, R. Grumbine, W. Higgins, H. Li, Y. Lin, G. Manikin, D. Parrish, and W. Shi. 2006. North American regional reanalysis. *B. Am. Meteorol. Soc.* 87 (3):343–360.

Millet, D. B., M. Baasandorj, L. Hu, D. Mitroo, J. Turner, and B. J. Williams. 2016. Nighttime chemistry and morning isoprene can drive urban ozone downwind of a major deciduous forest. *Environ. Sci. Technol. 50* (8):4335–4342.

Morris, G. A., S. Hersey, A. M. Thompson, S. Pawson, J. E. Nielsen, P. R. Colarco, W. W. McMillan, A. Stohl, S. Turquety, J. Warner, B. J. Johnson, T. L. Kucsera, D. E. Larko, S. J. Oltmans, and J. C. Witte. 2006. Alaskan and Canadian forest fires exacerbate ozone pollution over Houston, Texas, on 19 and 20 July 2004. *J. Geophys. Res.-Atmos.* 111 (D24).

MTBS. MTBS Data Search and Distribution Tools. http://www.mtbs.gov/data/customquery.html.

Natural Resources. 2016. The State of Canada's Forests: Annual Report 2016. Natural Resources, Canada. http://cfs.nrcan.gc.ca/pubwarehouse/pdfs/37265.pdf (Accessed November 7, 2016)

NEI, 2011. 2011 National Emission Inventory Data. U.S. Environmental Protection Agency, https://www.epa.gov/air-emissions-inventories/2011-national-emissions-inventory-nei-data.

Nelson, L. D., J. M. Garay, A. R. Kahn, and A. B. Dunst. 2013. Stereoscopic Height and Wind Retrievals for Aerosol Plumes with the MISR INteractive eXplorer (MINX). *Remote Sens.* 5 (9).

NIFC. 2016. Wildland fire summary and statistics annual report 2012. National Interagency Fire Centre. http://www.nifc.gov/

Ngan, F., H. Kim, P. Lee, K. Al-Wali, and B. Dornblaser. 2013. A study of nocturnal surface wind speed overprediction by the WRF-ARW model in southeastern Texas. *J. Appl. Meteorol. Clim.* 52 (12):2638–2653.

NOAA, Billion-dollar weather and climate disasters: Table of events. 2012a. National Centers for Environmental Information. https://www.ncdc.noaa.gov/billions/events (Accessed November 8, 2016)

NOAA. Wildfires-September 2012b. https://www.ncdc.noaa.gov/sotc/fire/201209 (Accessed November 6, 2016).

Novelli, P. C., K. A. Masarie, P. M. Lang, B. D. Hall, R. C. Myers, and J. W. Elkins. 2003. Reanalysis of tropospheric CO trends: Effects of the 1997–1998 wildfires. *J. Geophys. Res.-Atmos.* 108 (D15).

Pacifico, F., S. P. Harrison, C. D. Jones, and S. Sitch. 2009. Isoprene emissions and climate. *Atmos. Environ.* 43 (39):6121–6135.

Pan, S., Y. Choi, A. Roy, X. Li, W. Jeon, and A. H. Souri. 2015. Modeling the uncertainty of several VOC and its impact on simulated VOC and ozone in Houston, Texas. *Atmos. Environ.* 120:404–416.

Park, R. J., S. K. Hong, H. A. Kwon, S. Kim, A. Guenther, J. H. Woo, and C. P. Loughner. 2014. An evaluation of ozone dry deposition simulations in East Asia. *Atmos. Chem. Phys.* 14 (15):7929–7940.

Parrington, M., P. I. Palmer, D. K. Henze, D. W. Tarasick, E. J. Hyer, R. C. Owen, D. Helmig, C. Clerbaux, K. W. Bowman, M. N. Deeter, E. M. Barratt, P. F. Coheur, D. Hurtmans, Z. Jiang, M. George, and J. R. Worden. 2012. The influence of boreal biomass burning emissions on the distribution of tropospheric ozone over North America and the North Atlantic during 2010. *Atmos. Chem. Phys.* 12 (4):2077–2098.

Paugam, R., M. Wooster, S. Freitas, and M. Val Martin. 2016. A review of approaches to estimate wildfire plume injection height within large-scale atmospheric chemical transport models. *Atmos. Chem. Phys.* 16 (2):907–925.

Penner, J. E., L. C. Haselman, and L. L. Edwards. 1986. Smoke-plume distributions above large-scale fires-implications for simulations of nuclear winter. *J. Clim. Appl. Meteorol.* 25 (10):1434–1444.

Peppler, R. A., C. P. Bahrmann, J. C. Barnard, N. S. Laulainen, D. D. Turner, J. R. Campbell, D. L. Hlavka, M. D. Cheng, R. A. Ferrare, R. N. Halthore, L. A. Heilman, C. J. Lin, J. A. Ogren, M. R. Poellot, L. A. Remer, J. D. Spinhirne, K. Sassen, and M. E. Splitt. 2000. ARM Southern Great Plains Site Observations of the Smoke Pall Associated with the 1998 Central American Fires. *B. Am. Meteorol. Soc.* 81 (11):2563–2591.

Perring, A. E., A. Wisthaler, M. Graus, P. J. Wooldridge, A. L. Lockwood, L. H. Mielke, P. B. Shepson, A. Hansel, and R. C. Cohen. 2009. A product study of the isoprene+NO_3 reaction. *Atmos. Chem. Phys.* 9 (14):4945–4956.

Pfister, G. G., L. K. Emmons, P. G. Hess, R. Honrath, J. F. Lamarque, M. Val Martin, R. C. Owen, M. A. Avery, E. V. Browell, J. S. Holloway, P. Nedelec, R. Purvis, T. B. Ryerson, G. W. Sachse, and H. Schlager. 2006. Ozone production from the 2004 North American boreal fires. *J. Geophys. Res.-Atmos.* 111 (D24):D24S07.

Pitts, J. N., E. Sanhueza, R. Atkinson, W. P. L. Carter, A. M. Winer, G. W. Harris, and C. N. Plum. 1984. An investigation of the dark formation of nitrous acid in environmental chambers. *Int. J. Chem. Kinet.* 16 (7):919–939.

Poisson, N., M. Kanakidou, and P. J. Crutzen. 2000. Impact of non-methane hydrocarbons on tropospheric chemistry and the oxidizing power of the global troposphere: 3-dimensional modelling results. *J. Atmos. Chem.* 36 (2):157–230.

Pouliot, G., T. Pierce, W. Benjey, S. M. O'Neill, and S. A. Ferguson. 2005. Wildfire emission modeling: integrating BlueSky and SMOKE. 14th International Emission Inventory Conference, April 11–14 2005, Las Vegas, NV.

Prins, E. M., and W. P. Menzel. 1992. Geostationary satellite detection of bio mass burning in South America. *Int. J. Remote Sens.* 13 (15):2783–2799.

Raffuse, S. M., K. J. Craig, N. K. Larkin, T. T. Strand, D. Coe Sullivan, N. J. M. Wheeler, and R. Solomon. 2012. An evaluation of modeled plume injection height with satellite-derived observed plume height. *Atmosphere* 3 (1):103.

Reimann, S., P. Calanca, and P. Hofer. 2000. The anthropogenic contribution to isoprene concentrations in a rural atmosphere. *Atmos. Environ.* 34 (1):109–115.

Rogers, C. M., and K. P. Bowman. 2001. Transport of smoke from the Central American fires of 1998. *J. Geophys. Res.-Atmos.* 106 (D22):28357–28368.

Ryan, K. C., and T. S. Opperman. 2013. LANDFIRE – A national vegetation/fuels data base for use in fuels treatment, restoration, and suppression planning. *Forest Ecol. Manag.* 294:208–216.

Sahu, L. K., and P. Saxena. 2015. High time and mass resolved PTR-TOF-MS measurements of VOCs at an urban site of India during winter: Role of anthropogenic, biomass burning, biogenic and photochemical sources. *Atmos. Res.* 164–165:84–94.

Saide, P. E., S. N. Spak, R. B. Pierce, J. A. Otkin, T. K. Schaack, A. K. Heidinger, A. M. da Silva, M. Kacenelenbogen, J. Redemann, and G. R. Carmichael. 2015. Central American biomass burning smoke can increase tornado severity in the U.S. *Geophys. Res. Lett.* 42 (3):956–965.

Sakamaki, F., S. Hatakeyama, and H. Akimoto. 1983. Formation of nitrous acid and nitric oxide in the heterogeneous dark reaction of nitrogen dioxide and water vapor in a smog chamber. *Int. J. Chem. Kinet.* 15 (10):1013–1029.

Sarwar, G., S. J. Roselle, R. Mathur, W. Appel, R. L. Dennis, and B. Vogel. 2008. A comparison of CMAQ HONO predictions with observations from the Northeast Oxidant and Particle Study. *Atmos. Environ.* 42 (23):5760–5770.

Schneidemesser, E. V., P. S. Monks, V. Gros, J. Gauduin, and O. Sanchez. 2011. How important is biogenic isoprene in an urban environment? A study in London and Paris. *Geophys. Res. Lett.* 38 (19):L19804.

Seinfeld, J. H., and S. N. Pandis. 2006. *Atmospheric Chemistry and Physics: From Air Pollution to Climate Change*. 2nd ed. John Wiley, New York.

Sessions, W. R., H. E. Fuelberg, R. A. Kahn, and D. M. Winker. 2011. An investigation of methods for injecting emissions from boreal wildfires using WRF-Chem during ARCTAS. *Atmos. Chem. Phys.* 11 (12):5719–5744.

Sillman, S., M. A. Carroll, T. Thornberry, B. K. Lamb, H. Westberg, W. H. Brune, I. Faloona, D. Tan, P. B. Shepson, A. L. Sumner, D. R. Hastie, C. M. Mihele, E. C. Apel, D. D. Riemer, and R. G. Zika. 2002. Loss of isoprene and sources of nighttime OH radicals at a rural site in the United States: Results from photochemical models. *J. Geophys. Res.-Atmos.* 107 (D5–6).

Skamarock, W. C., J. B. Klemp, J. Dudhia, D. O. Gill, D. M. Barker, M. G. Duda, X.-Y. Huang, W. Wang, and J. G Powers. 2008. A description of the advanced research WRF version 3. Technical note NCAR/TN–475+STR, National Center for Atmospheric Research, Boulder, Colorado, U.S.A. http://www2.mmm.ucar.edu/wrf/users/docs/arw_v3.pdf (accessed December 24, 2015).

SMOKE, 2016. SMOKE v3.6.5 User's Manual. The University of North Carolina at Chapel Hill, North Carolina, United States.

Sofiev, M., R. Vankevich, T. Ermakova, and J. Hakkarainen. 2013. Global mapping of maximum emission heights and resulting vertical profiles of wildfire emissions. *Atmosp. Chem. Phys.* 13 (14):7039–7052.

Solmon, F., C. Sarrat, D. Serça, P. Tulet, and R. Rosset. 2004. Isoprene and monoterpenes biogenic emissions in France: Modeling and impact during a regional pollution episode. *Atmos. Environ.* 38 (23):3853–3865.

Song, J., W. Vizuete, S. Chang, D. Allen, Y. Kimura, S. Kemball-Cook, G. Yarwood, M.-A. Kiournourtzoglou, E. Atlas, A. Hansel, A. Wisthaler, and E. McDonald-Buller. 2008. Comparisons of modeled and observed isoprene concentrations in southeast Texas. *Atmos. Environ.* 42 (8):1922–1940.

Souri, A. H., Y. Choi, W. Jeon, X. Li, S. Pan, L. Diao, and D. A. Westenbarger. 2016. Constraining NOx emissions using satellite NO_2 measurements during 2013 DISCOVER-AQ Texas campaign. *Atmos. Environ.* 131:371–381.

Squire, O. J., A. T. Archibald, P. T. Griffiths, M. E. Jenkin, D. Smith, and J. A. Pyle. 2015. Influence of isoprene chemical mechanism on modelled changes in tropospheric ozone due to climate and land use over the 21st century. *Atmos. Chem. Phys.* 15 (9):5123–5143.

Stemmler, K., M. Ammann, C. Donders, J. Kleffmann, and C. George. 2006. Photosensitized reduction of nitrogen dioxide on humic acid as a source of nitrous acid. *Nature* 440 (7081):195–198.

Stutz, J., B. Alicke, R. Ackermann, A. Geyer, S. Wang, A. B. White, E. J. Williams, C. W. Spicer, and J. D. Fast. 2004. Relative humidity dependence of HONO chemistry in urban areas. *J. Geophys. Res.-Atmos.* 109 (D3):D03307.

Stutz, J., K. W. Wong, L. Lawrence, L. Ziemba, J. H. Flynn, B. Rappenglück, and B. Lefer. 2010. Nocturnal NO_3 radical chemistry in Houston, TX. *Atmos. Environ.* 44 (33):4099–4106.

Su, H., Y. Cheng, P. Cheng, Y. Zhang, S. Dong, L. Zeng, X. Wang, J. Slanina, M. Shao, and A. Wiedensohler. 2008. Observation of nighttime nitrous acid (HONO) formation at a non-urban site during PRIDE-PRD2004 in China. *Atmos. Environ.* 42 (25):6219–6232.

Svensson, R., E. Ljungström, and O. Lindqvist. 1987. Kinetics of the reaction between nitrogen dioxide and water vapour. *Atmos. Environ.* (1967) 21 (7):1529–1539.

Tai, E., M. Jimenez, O. Nopmongcol, G. Wilson, G. Mansell, B. Koo, and G. Yarwood. 2008. Boundary conditions and fire emissions modeling. ENVIRON International Corporation, Novato, CA, United States.

Tang, W., D. S. Cohan, G. A. Morris, D. W. Byun, and W. T. Luke. 2011. Influence of vertical mixing uncertainties on ozone simulation in CMAQ. *Atmos. Environ.* 45 (17):2898–2909.

Tanner, R. L., W. J. Parkhurst, M. L. Valente, K. L. Humes, K. Jones, and J. Gilbert. 2001. Impact of the 1998 Central American fires on PM2.5 mass and composition in the southeastern United States. *Atmos. Environ.* 35 (36):6539–6547.

Tong, S., S. Hou, Y. Zhang, B. Chu, Y. Liu, H. He, P. Zhao, and M. Ge. 2015. Comparisons of measured nitrous acid (HONO) concentrations in a pollution period at urban and suburban Beijing, in autumn of 2014. *Sci. China Chem.* 58 (9):1393–1402.

Tomback, D. F., J. K. Clary, J. Koehler, R. J. Hoff, and S. F. Arno. 1995. The effects of blister rust on post-fire regeneration of whitebark pine: The sundance burn of northern Idaho (U.S.A.). *Conserv. Biol.*, 9: 654–664.

Towne, E. G., and J. M. Craine. 2016. A critical examination of timing of burning in the Kansas Flint hills. *Rangeland Ecol. Manag.* 69 (1):28–34.

Val Martin, M., J. A. Logan, R. A. Kahn, F. Y. Leung, D. L. Nelson, and D. J. Diner. 2010. Smoke injection heights from fires in North America: analysis of 5 years of satellite observations. *Atmos. Chem. Phys.* 10 (4):1491–1510.

Val Martin, M., R. A. Kahn, J. A. Logan, R. Paugam, M. Wooster, and C. Ichoku. 2012. Space-based observational constraints for 1-D fire smoke plume-rise models. *J. Geophys. Res.-Atmos.* 117 (D22): D22204.

van der werf, G. R., J. T. Randerson, L. Giglio, G. J. Collatz, M. Mu, P. S. Kasibhatla, D. C. Morton, R. S. DeFries, Y. Jin, and T. T. van Leeuwen. 2010. Global fire emissions and the contribution of deforestation, savanna, forest, agricultural, and peat fires (1997–2009). *Atmos. Chem. Phys.* 10 (23):11707–11735.

Wagner, P., and W. Kuttler. 2014. Biogenic and anthropogenic isoprene in the near-surface urban atmosphere—A case study in Essen, Germany. *Sci. Total Environ.* 475:104–115.

Walter, C., S. R. Freitas, C. Kottmeier, I. Kraut, D. Rieger, H. Vogel, and B. Vogel. 2016. The importance of plume rise on the concentrations and atmospheric impacts of biomass burning aerosol. *Atmos. Chem. Phys.* 16 (14):9201–9219.

Wang, Y. H., D. J. Jacob, and J. A. Logan. 1998. Global simulation of tropospheric O_3-NOx-hydrocarbon chemistry 3. Origin of tropospheric ozone and effects of nonmethane hydrocarbons. *J. Geophys. Res.-Atmos.* 103 (D9):10757–10767.

Warner, J., M. M. Comer, C. D. Barnet, W. W. McMillan, W. Wolf, E. Maddy, and G. Sachse. 2007. A comparison of satellite tropospheric carbon monoxide measurements from AIRS and MOPITT during INTEX-A. *J. Geophys. Ress-Atmos.* 112 (D12): D12S17.

Wentzell, J. J. B., C. L. Schiller, and G. W. Harris. 2010. Measurements of HONO during BAQS-Met. *Atmos. Chem. Phys.* 10 (24):12285–12293.

Wiedinmyer, C., S. K. Akagi, R. J. Yokelson, L. K. Emmons, J. A. Al-Saadi, J. J. Orlando, and A. J. Soja. 2011. The Fire INventory from NCAR (FINN): a high resolution global model to estimate the emissions from open burning. *Geosci. Model Dev.* 4 (3):625–641.

Wiedinmyer, C., B. Quayle, C. Geron, A. Belote, D. McKenzie, X. Zhang, S. O'Neill, and K. Klos Wynne. 2006a. Estimating emissions from fires in North America for air quality modeling. *Atmos. Environ.* 40 (19):3419–3432.

Wiedinmyer, C., X. Tie, A. Guenther, R. Neilson, and C. Granier. 2006b. Future changes in biogenic isoprene emissions: How might they affect regional and global atmospheric chemistry? *Earth Interact.* 10 (3):1–19.

Wise, E. K. 2012. Hydroclimatology of the US intermountain west. *Prog. Phys. Geog.* 36 (4):458–479.

Willmott, C. J. 1981. On the validation of models. *Phys. Geogr.* 2 (2):184–194.

WRAP (Western Governors Association/Western Regional Air Partnership), 2005. 2002 fire emission inventory for the WRAP region-phase II. Air Sciences Inc. U.S.A. http://www.wrapair.org/forums/fejf/documents/WRAP_2002_PhII_EI_Report_20050722.pdf (Accessed November 8, 2016)

Xie, Y., F. Paulot, W. P. L. Carter, C. G. Nolte, D. J. Luecken, W. T. Hutzell, P. O. Wennberg, R. C. Cohen, and R. W. Pinder. 2013. Understanding the impact of recent advances in isoprene photooxidation on simulations of regional air quality. *Atmos. Chem. Phys.* 13 (16):8439–8455.

Xie, X., M. Shao, Y. Liu, S. Lu, C.-C. Chang, and Z.-M. Chen. 2008. Estimate of initial isoprene contribution to ozone formation potential in Beijing, China. *Atmos. Environ.* 42 (24):6000–6010.

Yan, X., T. Ohara, and H. Akimoto. 2006. Bottom-up estimate of biomass burning in mainland China. *Atmos. Environ.* 40 (27):5262–5273.

Yarwood, G., S. Rao, M. Yocke, and G. Z. Whitten. 2005. Updates to the Carbon Bond Chemical Mechanism: CB05. Rep. RT-04-00675, U. S. Environmental Protection Agency, Research Triangle Park, North Carolina, U.S.A. http://www.camx.com/publ/pdfs/cb05_final_report_120805.aspx (Accessed December 24, 2015).

Yurganov, L. N., W. W. McMillan, A. V. Dzhola, E. I. Grechko, N. B. Jones, and G. R. van der Werf. 2008. Global AIRS and MOPITT CO measurements: Validation, comparison, and links to biomass burning variations and carbon cycle. *J. Geophys. Res.-Atmos.* 113 (D9):D09301.

Zhang, L., J. R. Brook, and R. Vet. 2003. A revised parameterization for gaseous dry deposition in air-quality models. *Atmos. Chem. Phys.* 3:2067–2082.

Zhang, R., G. Sarwar, J. C. H. Fung, A. K. H. Lau, and Y. Zhang. 2011. Impact of nitrous acid chemistry on air quality modeling results over the Pearl River Delta region. *Atmos. Chem. Phys. Discuss.* 11 (5):15075–15117.

Ziemba, L. D., J. E. Dibb, R. J. Griffin, C. H. Anderson, S. I. Whitlow, B. L. Lefer, B. Rappenglück, and J. Flynn. 2010. Heterogeneous conversion of nitric acid to nitrous acid on the surface of primary organic aerosol in an urban atmosphere. *Atmos. Environ.* 44 (33):4081–4089.

Appendices

Appendix 1

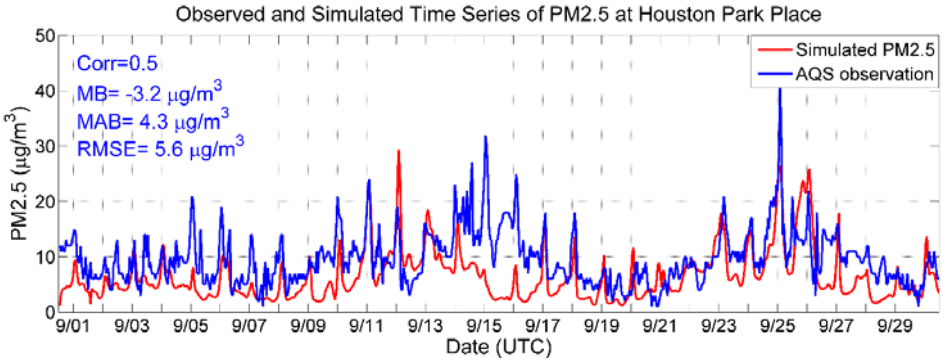

Fig. A1.1: Times series of $PM_{2.5}$ concentrations measured at Park Place station in September 2013.

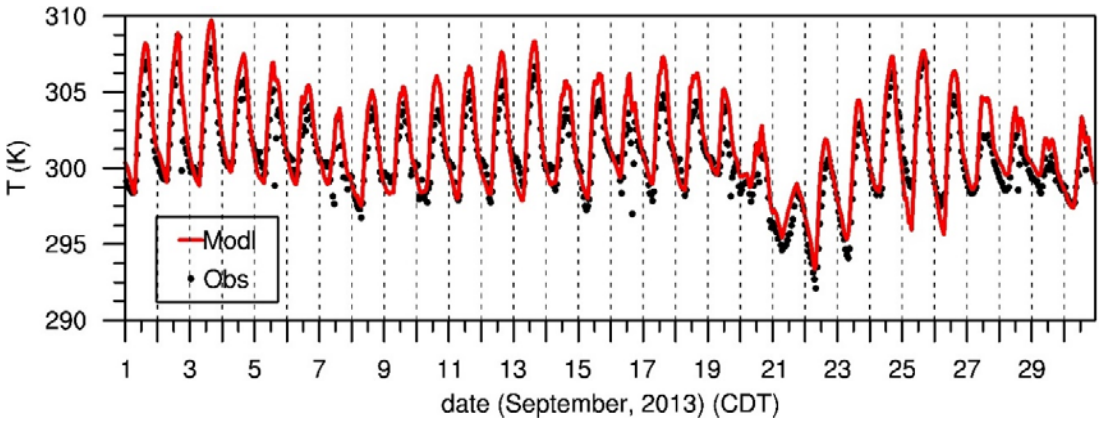

Fig. A1.2: Time series of observed and simulated temperature atop Moody Tower.

Table A1.1: Statistical summary of temperature model predictions. N represents the number of points, RHO the correlation coefficient, MML the model mean, MOB the observation mean, ME the mean error, MAE the mean absolute error, RMSE the root-mean-squared error and IOA the index of agreement.

T	N	RHO	MML (K)	MOB (K)	ME (K)	MAE (K)	RMSE (K)	IOA
Base	714	0.92	301.60	300.76	0.84	1.13	1.43	0.94

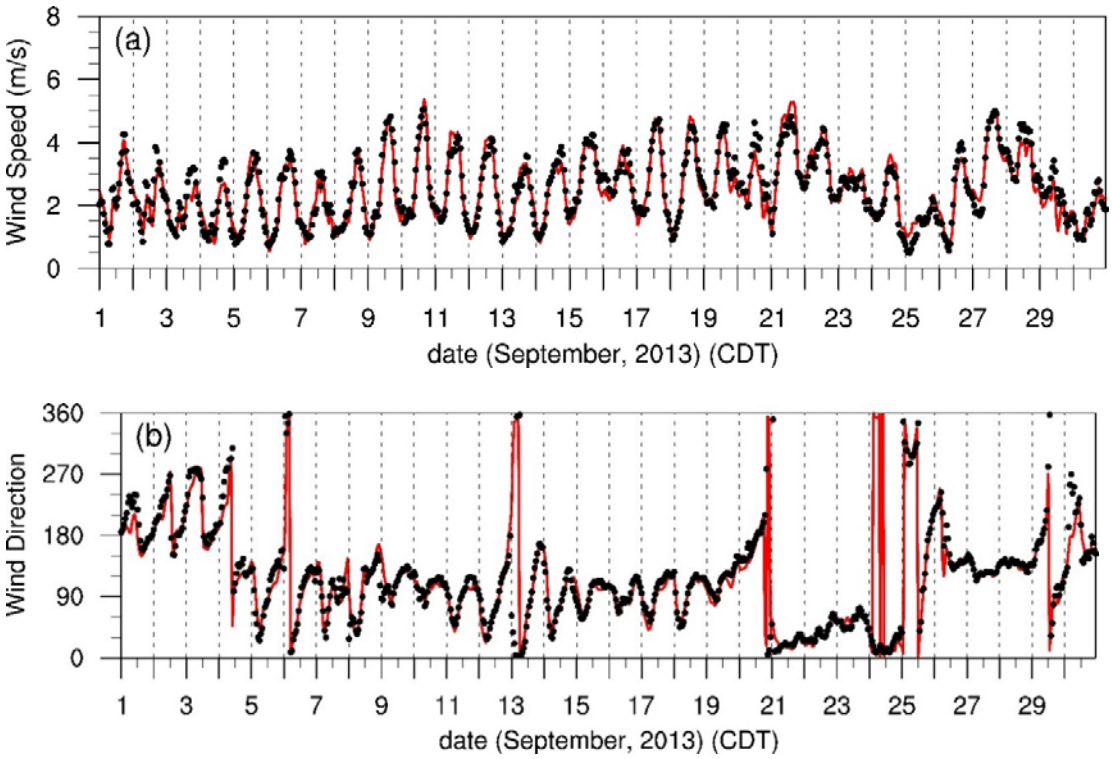

Fig. A1.3: Comparisons of model mean resultant wind speeds and directions with observations averaged over 46 TCEQ CAMS sites. (a) wind speed; (b) wind direction.

Resultant wind is the addition of all five-minute wind vectors in one hour. The resultant wind direction is the direction of the final vector, and the resultant wind speed is the final vector magnitude divided by the number of all vectors.

Table A1.2: TCEQ CAMS domain-wide statistical summary of model simulation of all day u- and v-wind components in September 2013.

wind	N	RHO	MML (m/s)	MOB (m/s)	ME (m/s)	MAE (m/s)	RMSE (M/S)	IOA
u-component	31710	0.84	-1.47	-1.40	-0.08	0.74	0.95	0.89
v-component	31710	0.84	0.31	0.44	-0.13	0.85	1.09	0.90

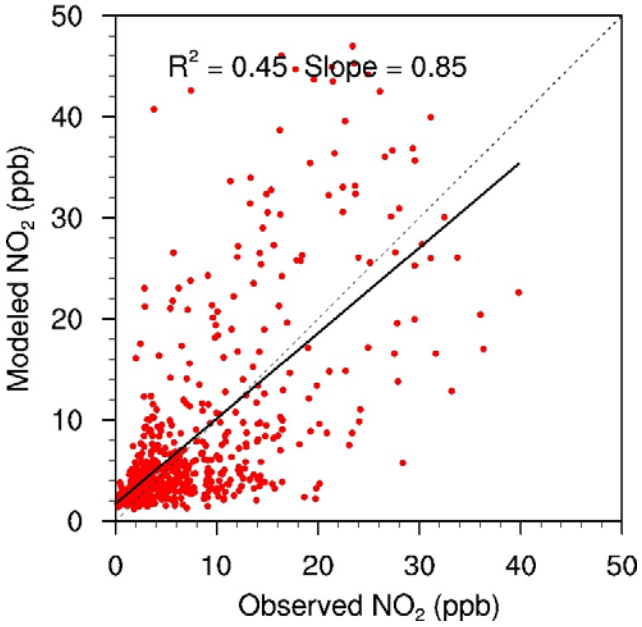

Fig. A1.4: Scatter plot of NO_2 from measurements atop UH's Moody Tower and CMAQ model simulation for September 2013. The thick solid line is the linear regression line and the thin dotted line is 1:1 line. The slope of the regression is 0.85 and coefficient of determination (R^2) 0.45.

Appendix 2

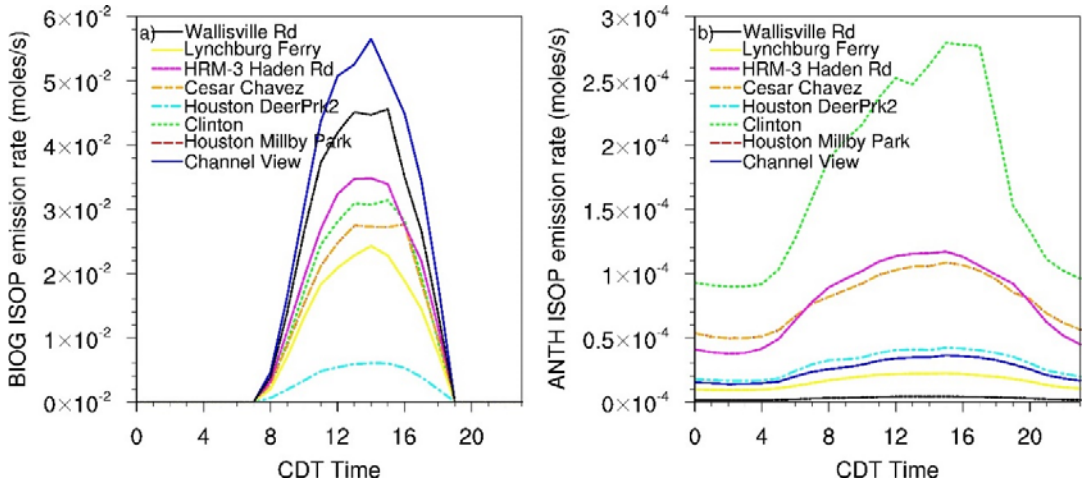

Fig. A2.1: Monthly mean diurnal variations of the isoprene emission rates in September 2013 based on NEI 2011 at eight TCEQ AutoGC stations. **(a)** Biogenic emissions; **(b)** anthropogenic emissions including various sectors. The lines of the Houston Milby Park and Cesar Chavez are overlapped because of their co-location of the same model grid cell.

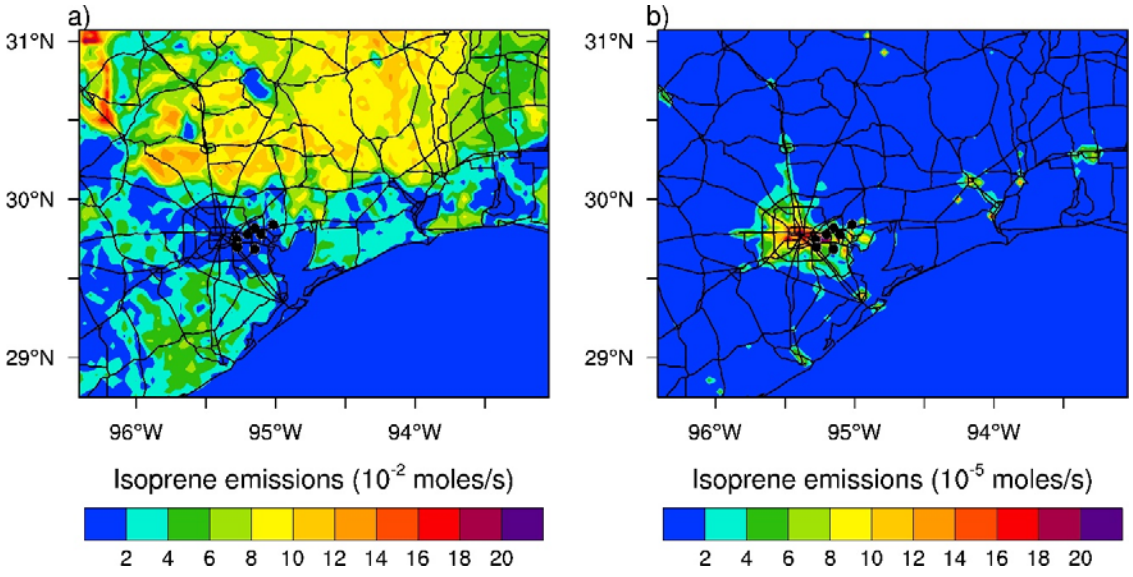

Fig. A2.2: Spatial distribution of monthly mean isoprene emission rates around Houston. Black dots represent the locations of eight TCEQ AutoGC sites. **(a)** Biogenic emissions in 10^{-2} moles/s; **(b)** anthropogenic emissions in 10^{-5} moles s^{-1}.

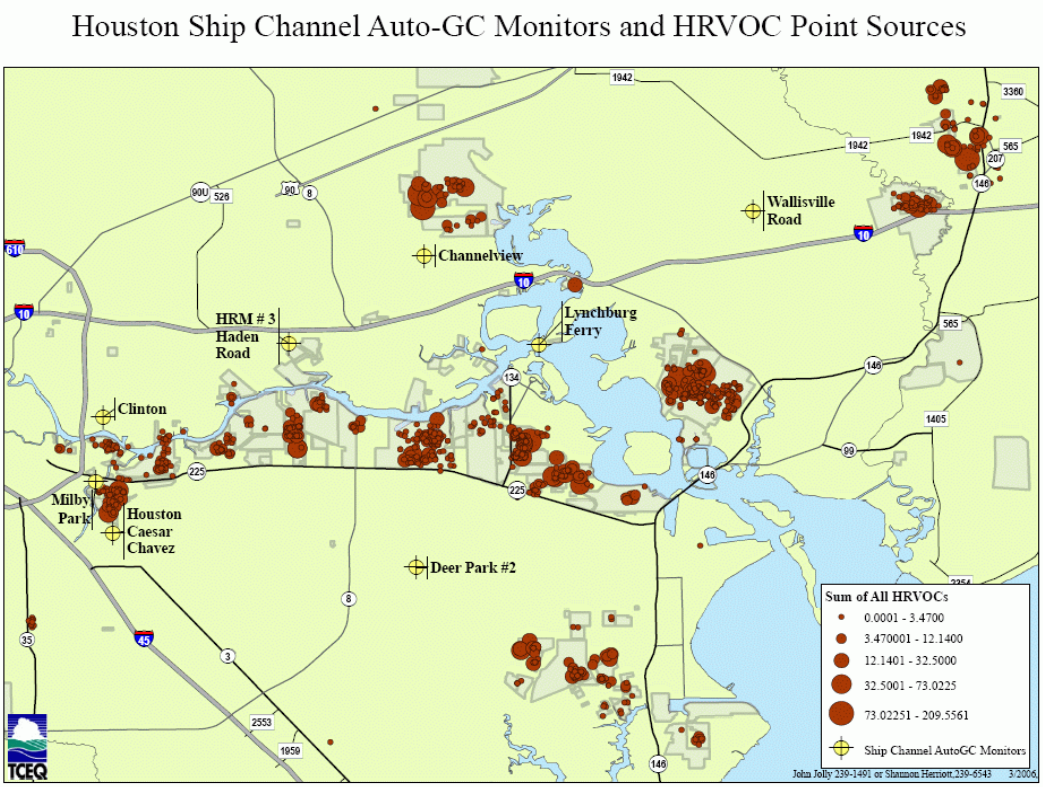

Fig. A2.3: Map of AutoGC monitors and point emission sources around Houston Ship Channel. Adopted from Estes M, C. Harper, J. Smith, W. Zhao, and D. Karp, 2008. Performance evaluation of isoprene in ozone modeling of Houston. The 7th Annual CMAS conference, Chapel Hill, NC, U.S.A.

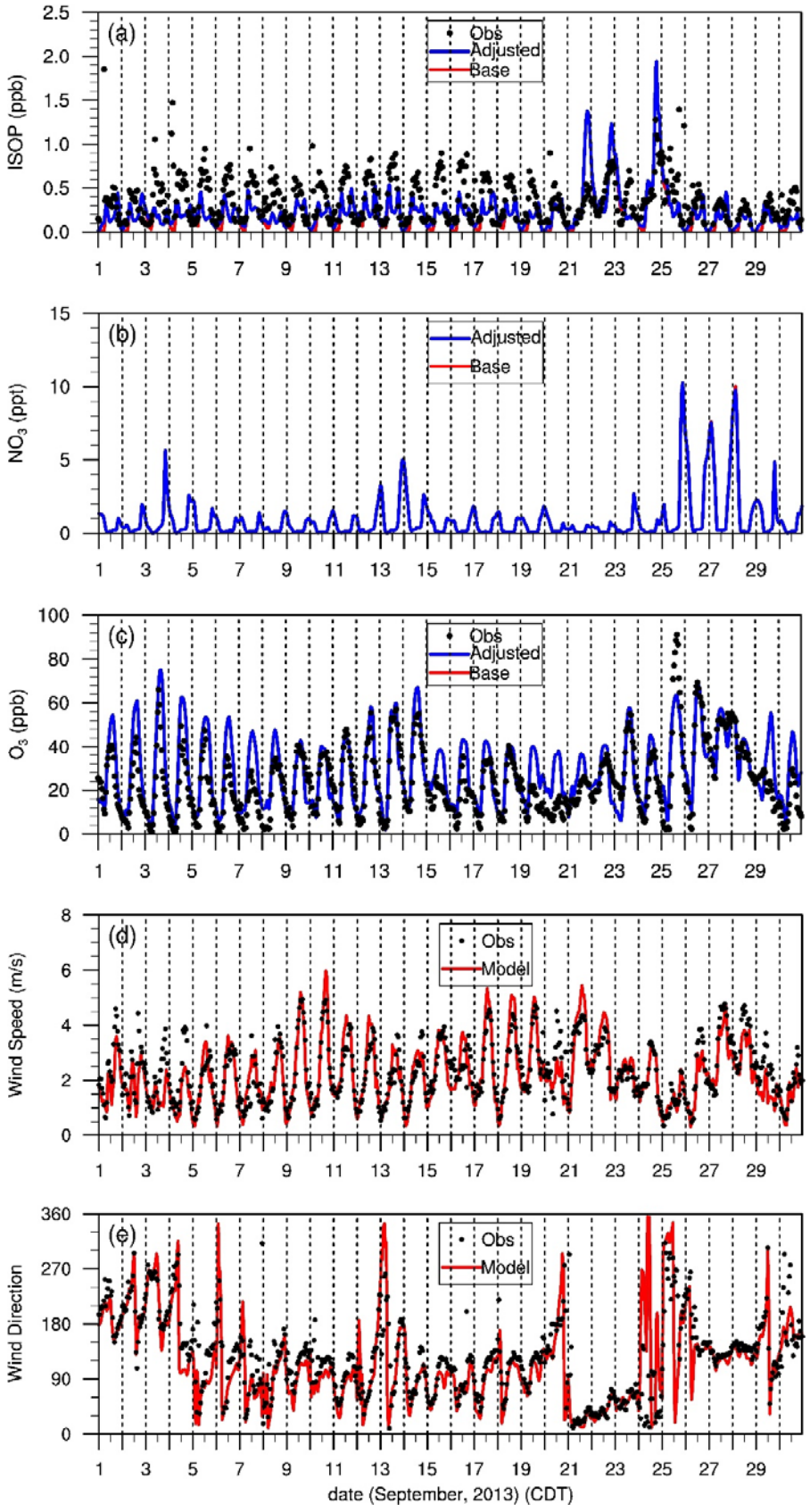
(a)
Obs
Adjusted
Base
ISOP (ppb)
2.5
2.0
1.5
1.0
0.5
0.0
(b)
Adjusted
Base
NO3 (ppt)
15
10
5
0
(c)
Obs
Adjusted
Base
O3 (ppb)
100
80
60
40
20
0
(d)
Obs
Model
Wind Speed (m/s)
8
6
4
2
0
(e)
Obs
Model
Wind Direction
360
270
180
90
0
1 3 5 7 9 11 13 15 17 19 21 23 25 27 29
date (September, 2013) (CDT)

Fig. A2.4: Time series of selected hourly trace gases and meteorological parameter observed and modeled (base and adjusted isoprene emission cases) in September 2013 averaged over the AutoGC network. **(a)** Isoprene; **(b)** NO_3 (no observation); **(c)** O_3; **(d)** Resultant wind speed (no adjusted emission case); (e) Resultant wind direction (no adjusted emission case).

The measured wind variables are resultant wind speed and direction. The resultant wind speed is the addition of all five-minute wind vectors in one hour. The resultant wind direction is the direction of the final vector, and the resultant wind speed is the final vector magnitude divided by the number of all vectors.

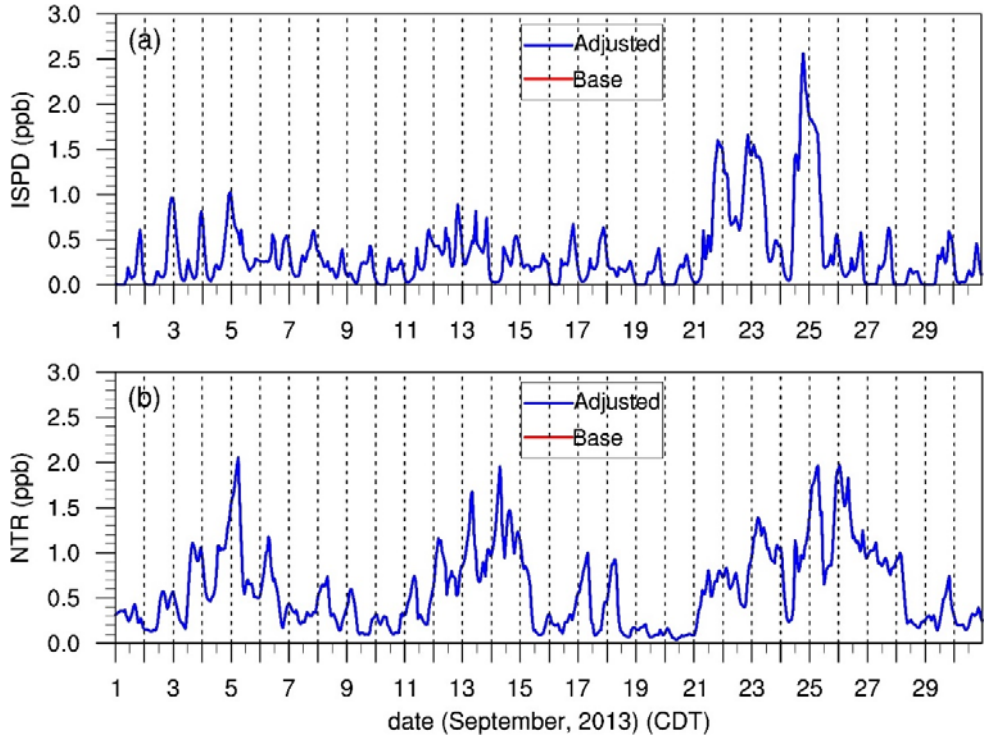

Fig. A2.5: Time series of selected hourly trace gases modeled (base and adjusted isoprene emission cases) in September 2013 averaged over the AutoGC network. **(a)** Isoprene oxidation products ISPD (methacrolein (MACR) and methyl vinyl ketone (MVK)); **(b)** gas phase organic nitrates (NTR).

Appendix 3

Table A3.1: Mapping of MOZART-4 species to CMAQ CB05 species.

CMAQ	MOZART-4
NO	NO
NO2	NO2
CO	CO
FORM	CH2O
ALD2	CH3CHO
ALDX	GLYALD
ETOH	C2H5OH
MEOH	CH3OH
ETHA	C2H6
PAR	C3H6 + 1.7*BIGENE + 5.0*BIGALK + 1.5*C3H8 +3.0*CH3COCH3 + 4.0*MEK + 1.0*C2H2 + 3.0*HYAC
ETH	C2H4
OLE	C3H6 + BIGENE
ISOP	ISOP
TERP	C10H16
TOL	0.3*TOLUENE
XYL	0.1*TOLUENE
BENZENE	0.6*TOLUENE
NR	C2H2 + 1.5*C3H8 + 0.5*TOLUENE + 0.3*BIGENE
CH4	CH4
SO2	SO2
NH3	NH3
PEC	BC
POC	OC
PMC	PM10 – PM25
PNO3	0.33*(PM25 – OC – BC)
PSO4	0.33*(PM25 – OC – BC)
PMOTHR	0.33*(PM25 – OC – BC)

(a) August 14, 2012

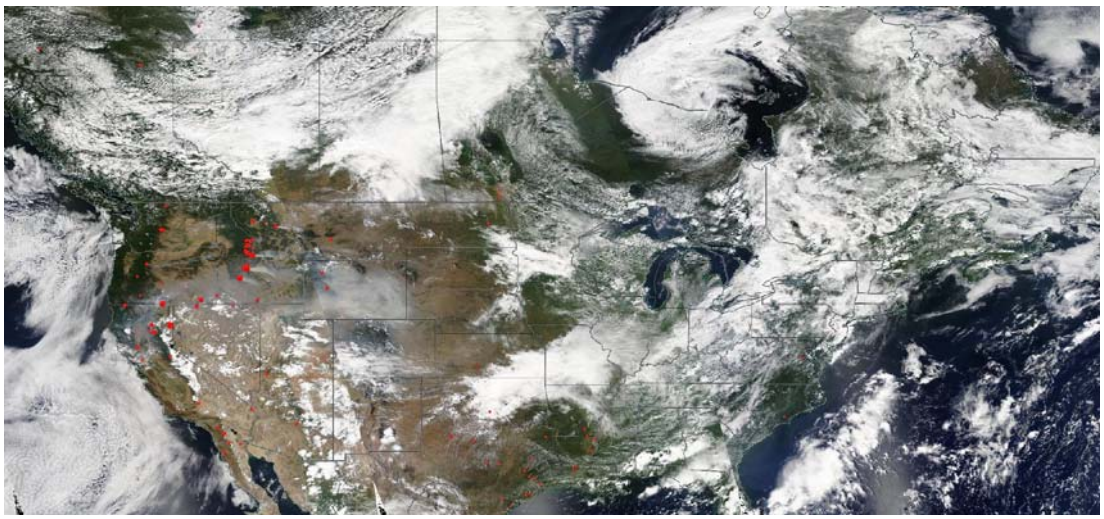

(b) August 15, 2012

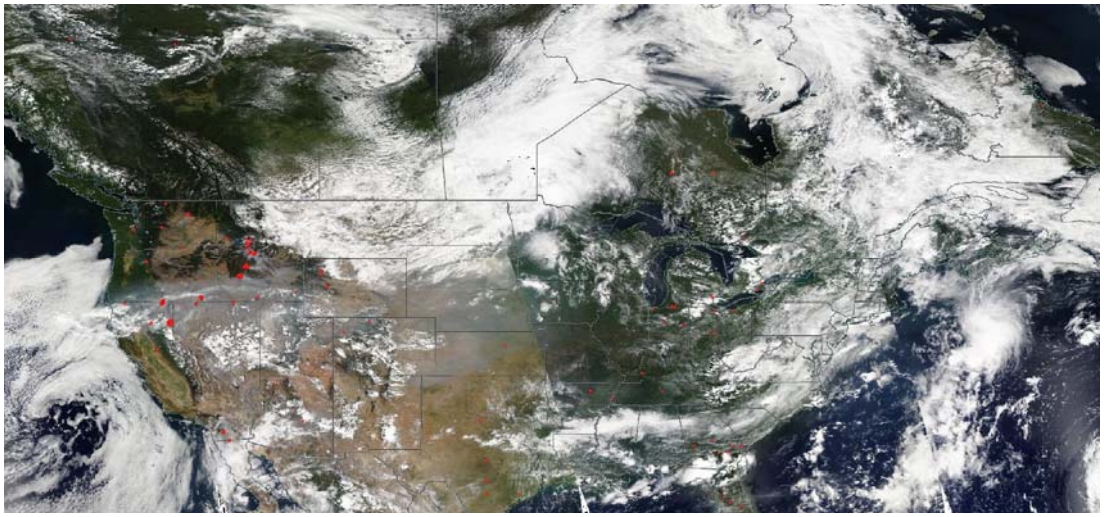

(c) August 16, 2012

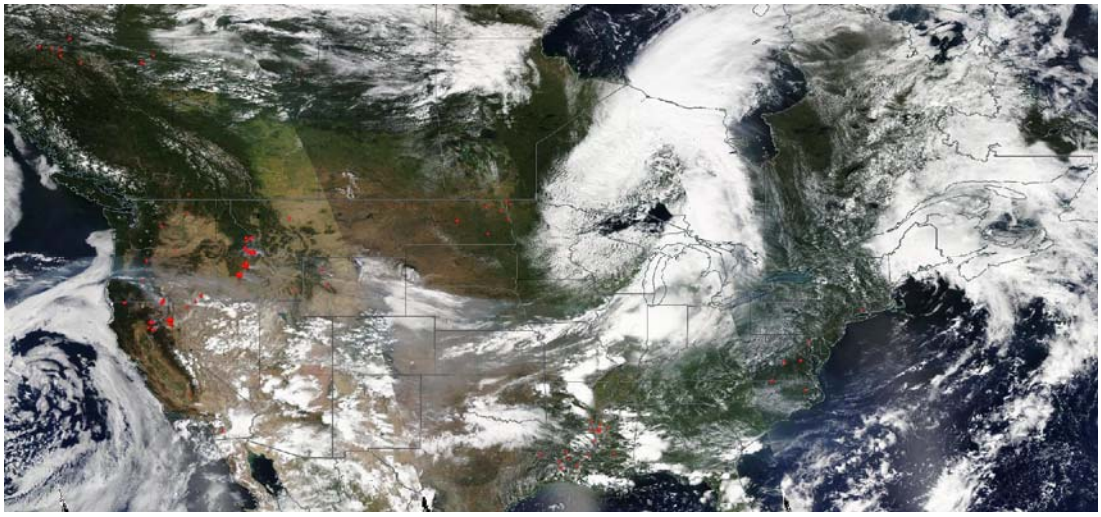

Fig. A3.1: Aqua/MODIS true color images acquired on **(a)** August 14; **(b)** August 15; **(c)** August 16, 2012 showing smoke from the western U.S. wildfires drifting eastward. Red dots represent Aqua/MODIS fire and thermal anomalies. The images were downloaded from NASA's EOSDIS worldview website at https://worldview.earthdata.nasa.gov

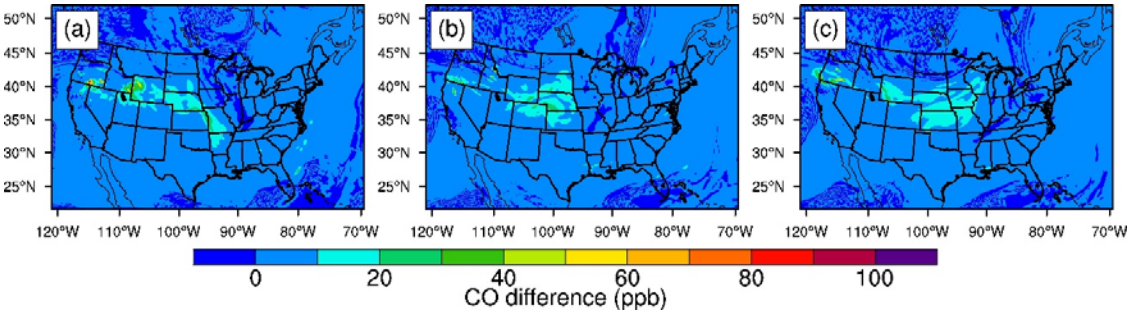

Fig. A3.2: CO concentration differences between simulations with and without biomass burning emissions at 500 hpa. The time is at **(a)** 10:00Z on Aug 14, 2012 **(b)** 20:00Z on Aug 15, 2012 **(c)** 8:00Z on Aug 16, 2012.